LEVEL

⟨12⟩

Report ONR-N00014-79-C-0418

SEA ICE MOVEMENTS FROM SYNTHETIC APERTURE RADAR

David A. Rothrock
Alan S. Thorndike
University of Washington
Polar Science Center
4057 Roosevelt Way NE
Seattle, Washington 98105

1 December 1981

DTIC
ELECTE
DEC 3 0 1981
H

Final Report for Period 1 April 1979 – 30 June 1981

AD A109002

DTIC FILE COPY

REPORT DOCUMENTATION PAGE		READ INSTRUCTIONS BEFORE COMPLETING FORM
1. REPORT NUMBER	2. GOVT ACCESSION NO. $AD-110900$ 2	3. RECIPIENT'S CATALOG NUMBER
4. TITLE (and Subtitle) SEA ICE MOVEMENTS FROM SYNTHETIC APERTURE RADAR		5. TYPE OF REPORT & PERIOD COVERED Final Technical Report 4/1/79-6/30/81
		6. PERFORMING ORG. REPORT NUMBER
7. AUTHOR(s) D. A. Rothrock A. S. Thorndike		8. CONTRACT OR GRANT NUMBER(s) N00014-79-C-0418
9. PERFORMING ORGANIZATION NAME AND ADDRESS Univ. of Washington, Polar Science Center 4057 Roosevelt Way NE Seattle, WA 98105		10. PROGRAM ELEMENT, PROJECT, TASK AREA & WORK UNIT NUMBERS NR307-428
11. CONTROLLING OFFICE NAME AND ADDRESS Office of Naval Research Arctic Programs, Code 428 Arlington, VA 22217		12. REPORT DATE 1 December 1981
		13. NUMBER OF PAGES 87
14. MONITORING AGENCY NAME & ADDRESS(if different from Controlling Office)		15. SECURITY CLASS. (of this report) Unclassified
		15a. DECLASSIFICATION DOWNGRADING SCHEDULE

16. DISTRIBUTION STATEMENT (of this Report)

Approved for public release; distribution unlimited.

17. DISTRIBUTION STATEMENT (of the abstract entered in Block 20, if different from Report)

18. SUPPLEMENTARY NOTES

19. KEY WORDS (Continue on reverse side if necessary and identify by block number)

Sea ice Synthetic Aperture Radar
Velocity SEASAT
Displacement

20. ABSTRACT (Continue on reverse side if necessary and identify by block number)

The spatial structure of the sea ice velocity field determines ridging, open water production and ice stress. The velocity has been measured roughly every 2 km along an 865 km track from SEASAT synthetic aperture radar. The movement shows individual pieces as large as 100 km. The spatial autocorrelation function of velocity has been estimated from these data and FGGE and AIDJEX buoy data, and has a length scale of roughly 1000 km. A model of the movement of a set of pieces shows the large uncertainty in opening and ridging estimated from velocities measured at only three points.

DD $_{1 JAN 73}^{FORM}$ 1473 EDITION OF 1 NOV 65 IS OBSOLETE
S/N 0102-LF-014-6601

TABLE OF CONTENTS

INTRODUCTION

Sea ice is affected by ice motion in two ways: first, the velocity advects ice from one region to another, and second, the deformations associated with spatial differences in velocity are important to the heat balance--through open water formation--and to the momentum balance--through ridging and ice stress. This report describes research applicable to both aspects of ice motion, but concentrating on the spatial structure of the velocity field and what this structure tells us about deformation.

The work is described in three parts. The first is the measurement of ice displacement from synthetic aperture radar (SAR) on the SEASAT satellite. The important feature of these measurements is their high spatial density-- 2 km intervals along an 865 km track--which, clearly shows for the first time the motion of distinct, rigid pieces of ice or floes. These measurements show the difficulty--or at least the arbitrariness--in defining a velocity derivative. The second subject is the analysis of these data and FGGE buoy data to provide the spatial autocorrelation function of the velocity field and to show how it is related to experiment design and the notion of (spatial) velocity derivatives. Last, a model of the velocity field as the motion of a set of pieces shows the uncertainty in estimating the amount of opening or ridging in an ice cover from velocity measurements at only a few points, as was done for instance during AIDJEX.

Two papers in which these subjects are discussed in detail are presented as appendices. Appendix A is a paper by Hall and Rothrock on the SAR measurement technique and data. It has been published in the *Journal of Geophysical Research*. Appendix B is a paper by Thorndike on ice kenematics. It defines the spatial autocorrelation function, evaluates it from the SAR and buoy data and describes the model of the piece-like velocity field; it will appear as a chapter in a NATO volume on Air-Sea-Ice Interaction.

DISPLACEMENT MEASUREMENTS FROM SEASAT SAR

The objective is to compare two images of the same ice taken at two different times and to estimate the movement of the ice during the time interval. The difficulty is in establishing the relative location of the two images. Our procedure was to use images from two nearly identical orbits and to align the two images by comparing the portions over land. No effort was made to establish absolute position.

The displacement from 5 October to 8 October 1978--or equivalently, the average velocity over the three day interval--was measured at points spaced about every two kilometers along a line 865 km long in the Beaufort Sea. Figures 1 and 2 in Appendix A show the location of the images and the data. Both components of displacement are presented as a function of distance along track. The motion of individual pieces is evident in the figures and can in fact be found by fitting piece-wise rigid body velocity profiles to the data. The movement of several pieces is shown in Figure 3 of Appendix A.

The along track component of displacement has an error which is zero at the coast growing to about 3 km at the far end of the strip. This error is due to stretching in the optical processor and could be reduced by choosing strips with land in both ends (our strip included Banks Island but stopped short of Siberia). The across track component of displacement has an error of 0.4 km. This error could be reduced by use of orbital data and by correcting for the slant range distortion. We recommend these improvements be made in future work with this type of data.

VELOCITY FIELD STRUCTURE

The autocorrelation function tells how similar the velocities are at two points a distance r apart. If r is as small as a few kilometers, the two velocities are nearly the same; so their correlation is unity. At large r, the two velocities are unrelated--zero correlation. The autocorrelation is described by two functions of r. Suppose the two points lie on the x-axis. $B_{||}(r)$ is the correlation of the x velocity components, and $B_{\perp}(r)$, the y components.

$$x = 0 \quad \xrightarrow{\;u(o)\;} \qquad x = r \quad \xrightarrow{\;u(r)\;} \qquad B_{||}(r) = \overline{u(o)u(r)}$$

$$v(o) \uparrow \qquad\qquad v(r) \uparrow \qquad\qquad B_{\perp}(r) = \overline{v(o) \cdot v(r)}$$

$$x = 0 \qquad\qquad x = r$$

-2-

These functions have been evaluated from AIDJEX and FGGE buoy data and are shown in Figure 16 of Appendix B. The notable feature is that the correlation length scale is about 1,000 km.

These functions have several uses. In experiment design they allow one to choose an economical sample spacing precluding either redundant data or data gaps. They can be used to estimate interpolation errors for a given data set (see §5.3.3.2 of Appendix B). One can estimate from them statistics of deformational quantities involving spatial velocity differences (see §5.4.2 and .3 of Appendix B).

The notion of the velocity gradient $\partial u/\partial x$ has been central to sea ice modeling, yet there is some difficulty in defining this quantity. A derivative is normally defined as a limit $\lim_{h \to 0} \dfrac{u(x + h) - u(x)}{h}$, but the SAR data (Figure 12 of Appendix A) show that such a limit does not exist everywhere, and where it does exist it describes the rotation of a floe, not a "large scale" gradient. The derivative exists in the mean squared sense, if

$$E \lim_{h \to 0} \left[\frac{u(x + h) - u(x)}{h}\right]^2 = c = \text{a constant}$$

where E is the expected value operator. The existence of the limit is equivalent to

$$\text{variance} \left[u(x + h) - u(x)\right] \sim ch^{\alpha}, \text{ as } h \to 0$$

with $\alpha = 2$. The SAR data, plotted in Figure 19 of Appendix B give $\alpha = 1.3$ for u ($\alpha = 1.1$ for v), giving further evidence that the velocity is too irregular spatially for a good derivative to exist.

The lack of a derivative can be circumvented in two ways. The average derivative over some region x can be evaluated as an integral of some velocity component around the boundary of the region. The autocorrelation functions then allow one to evaluate the error introduced by estimating that integral with only a few (buoy) data points. (See §5.4.5 of Appendix B.) It is important, though, to remember that the value of the average derivative depends on the size of the sampling region.

Alternatively, one can replace the notion of derivative with velocity *differences*. (See §5.4.2 of Appendix B.) Velocity differences exist without question; they can naturally be associated with strain rates, and their covariances can be estimated from $B_{||}$ and $B_{\perp}$.

MODEL OF THE PIECE-LIKE VELOCITY FIELD

The velocity field is demonstrably the movement of rigid pieces. A model incorporating this feature can be used to examine the practice of estimating opening and closing (ridging) from velocities measured at three or four points. We take the pieces to be defined by a random set of lines (a Poisson field); the average piece size of 16 km is taken from the SAR data. The differential movement of the pieces is given a Gaussian distribution. Many realizations of this motion are simulated. For each, the total opening (and closing) at the floe boundaries is plotted versus a "large scale" estimate of deformation made from the velocity at three points. Each realization gives one data point. The ensemble of points is shown in Figure 24 of Appendix B. The scatter shows how poorly a three point strain rate estimate allows us to determine the actual small scale opening and closing. A better parameterization would account for the scatter.

RECOMMENDATIONS FOR FUTURE WORK

Considerably more can be done with SEASAT SAR.

1) Further assessment of errors and tests of algorithms for eliminating errors should be made by examining pairs of strips over land. Strips a thousand kilometers long over the Canadian archipelago would be suitable. One would treat the strips as if they were over ice with land in each end, and apply all corrections for slant range distortion, orbital differences and stretching by the optical processor and then test the central portion of the strip to assess the remaining positioning errors.

2) SAR ice displacement measurements should be made to extend the present measurement back into the summer season. One might expect substantial seasonal variations in the sizes of pieces and the variance of the motion.

3) A sequence of three or more SAR strips should be analyzed to assess the persistence of floe boundaries. Do the velocity jumps occur at the same floe boundaries for weeks, or do floe boundaries change after several days?

The answer is relevant to parameterizing opening and closing in terms of sparse velocity measurements.

Other new work could include:

4)   The spatial velocity autocorrelations should be computed for the 1980 Arctic buoy data.

5)   The random piece-like velocity field model predicts considerable uncertainty in our estimates of open water formation and ridging based on velocity measurements. The implication is that the thickness distribution and heat flux estimates have a similar uncertainty, which has not yet been evaluated.

APPENDIX A

SEA ICE DISPLACEMENT FROM
SEASAT SYNTHETIC APERTURE RADAR

by R. T. Hall and D. A. Rothrock

ABSTRACT

Images obtained by a synthetic aperture radar on SEASAT have been used to measure sea ice displacements over a three day interval in October 1978. The position of a natural ice feature was measured on 5 October and again on 8 October; the difference in these two positions is a displacement. The displacement of many features was measured. The tracked features lie roughly along a line and are quite dense--about 2 km apart--over a distance of 865 km. The displacements are about twenty kilometers. Displacement errors grow with distance from shore becoming as large as 3 km. The graph of displacement versus distance has occasional discontinuities of several kilometers. Displacement discontinuities are accurate to ± 0.07 km along track and 3% of their magnitude across track.

INTRODUCTION

The motion of sea ice varies on all scales up to 10^3 km. The larger scale motions are driven by atmospheric pressure systems. On scales less than about 10^2 km the motion is affected by individual ice floes. The motion has traditionally been observed by tracking particles of ice: a couple of drifting manned camps, or a few buoys or radar reflectors. Each tracer is costly, limiting any experiment to on the order of ten points. Such methods do not reveal the spatial structure of the field of motion. What is needed are records thousands of kilometers long, sampled every kilometer or so.

Tracking natural ice features in satellite imagery improves the sampling rate. Following recognizable leads in LANDSAT visual photographs can provide records over 500 km long with about 25 irregularly spaced data points--an average spacing of 20 km [Nye, 1975]. Synthetic aperture radar (SAR) has the potential to provide yet more dense measurements. Its high resolution and sensitivity to surface roughness allow individual roughness features to be tracked, and these are more abundant than new leads.

The last decade has seen a considerable amount of radar imagery collected from aircraft. Airborne imaging radar data from 1975 was used to provide ice

displacements at spacings of about 10 km over an area roughly 10^4 km^2 [*Bryan et al.* 1977; *Leberl et al.* 1979]. But in general the distortion caused by the wide look angle and the aircraft motion discouraged quantitative analysis. It was not until generous amounts of quasi-corrected imagery from the L-band SAR on SEASAT became available through NOAA that the general sea ice community could experience firsthand the tantalizing potential of radar data.

This paper describes a technique for measuring ice displacements from these SAR images. It is not intended to be a comprehensive analysis of the performance of the system, but rather a report on some encouraging results. Measurements are presented of both components of displacement versus a single horizontal coordinate. This data record is 865 km long and has 417 data points--roughly one point every 2 km. Measurement errors are assessed by applying the same method to images of land where there are no displacements. The errors are discussed in terms of the satellite system and the optical data processing procedure. It appears that SEASAT SAR can provide 3 day displacements accurate to several kilometers and displacement discontinuities accurate to one or two hundred meters. With sufficient care, these errors could be reduced.

THE DATA

SEASAT operated from early July until 10 October 1978, collecting SAR data over swaths 100 km wide. More than 10^5 km of arctic data were collected, half of this over sea ice in the Beaufort, Chuckchi and East Siberian Seas south of 75°N. Often the sensor was turned on over North America, crossed the Arctic Ocean and was turned off over Siberia. Hence, there is often land at both ends of the swath which can be used both to eliminate some errors in the data and to assess those errors remaining.

The novel feature of SAR is that it combines data taken at different positions along the flight path to synthesize a radar image from an antenna much larger than actually used—thus providing the high resolution. [See, for example, *Harger*, 1970, or *Reeves*, 1975.] The data are transmitted from the satellite and stored in digital format. The synthesis of the bulk of this high resolution data is presently performed by the Jet Propulsion Laboratory in Pasadena by an optical rather than digital process. The 100 km swath is processed as four adjacent 25 km swaths. The scale is 1:500,000; hence, two millimeters on the film strip represent a distance of one kilometer. The resolution of our images is about 0.035 km on the ground; 0.07 mm on the film. The film strips are 70 mm positive transparencies. Not all are of good quality: we received one strip with a systematic blurring and elongation of features and another with double images for each pixel. The technical details of the SEASAT SAR system are reviewed by *Jordan* [1980].

These images of sea ice look much like visual photographs. Many familiar shapes and structures can be seen: leads, floes, and ridges. The same shapes are clearly recognizable in views of the same ice taken at different times. The correspondence, however, between radar and visual images is not always consistent [see, for example, *Bryan*, 1976].

To measure displacement, one needs to know the position of a recognizable ice feature imaged from two successive orbits. Since there was no control on absolute location, we chose to use orbits three days apart (or a multiple of three) because these orbits are almost identical. We examined in detail orbits 1396, 1439, and 1482 on October 2, 5 and 8, knowing from NOAA VHRR images that there was ice movement during this period, and wanting the most winter-like ice conditions. The data reported here are drawn from the latter two orbits. The ground swath is shown in Figure 1. Furthermore, we looked only at features roughly in the center of a single 25 km swath, thus avoiding any need to register the adjacent film strips and also minimizing the effect of slant-range distortion.

MEASUREMENT TECHNIQUE

To identify features in two successive images, and to find their initial and subsequent positions in a common coordinate system, we have used a Bendix Analytical Plotter Model C. This machine normally functions as a stereographic mapping tool; we have used it as an x,y digitizer with the crucial feature that two images can be viewed simultaneously. A few guide lines are drawn on the images to help keep the viewer oriented as he searches for features. The two images are placed on the two viewing stages of the plotter, and the stages are independently moved until the two cursors are located on the same feature in both images. The x,y coordinates of the cursor positions relative to the viewing stages are then recorded. With this equipment. one can measure about twenty-five data points in an hour.

Since the Bendix plotter is designed to accept 24 cm x 24 cm aerial photographs, our long film strips had to be analyzed piecemeal in overlapping segments representing roughly 100 km of ground coverage. To reassemble the data from the segments into one long data record, two reference points were marked in the overlapped regions of each pair of adjacent segments and measured in both reference frames. Thus, the data from each segment could be translated into the reference frame of the previous segment, and the segments reassembled into one long record.

The coordinate system is defined by a combined use of time marks and land. The time marks are dots spaced along the edges of the film strip. They define both the inboard and outboard edge of the 25 km ground swath even though the imagery may extend a bit outside them. They would also define distance along track except for some glitch in the system. Our x-axis is taken to run through the inboard time marks on both images. The y-axis is perpendicular to x through the most westerly land feature on Banks Island.

Ice displacements (u,v) from initial positions (x,y) are plotted in Figure 2 versus x only. The data disclose the motion of individual pieces of ice. Each piece has a solid body rotation and translation; between pieces are jumps in displacement. Figure 3 illustrates this by showing a line drawn from the first to the last point on each piece both before and after the displacement. We see rotations of several degrees, translations of ten to twenty-five kilometers, and displacement jumps up to several kilometers.

These data resolve the discontinuous nature of the field of motion, and they do so over a great enough distance to show many jumps. Thus we now have a data set from which to theorize about the structure of the ice displacement field and how the discontinuities in it change the ice cover. The opening and closing of leads, however, cannot be obtained directly from this one dimensional slice of a two dimensional displacement field. They require the component of a displacement jump normal to a line of discontinuity (or crack or lead), and we have not measured the directions of these lines. In fact, these directions are not well defined on the images.

Plots of the quantities shown in Figure 2 were made to the same scale as the image to see what correspondence there was between leads and displacement jumps. The leads of this October scene are not the meandering angular lines of April ice, but are more lacy like the open water surrounding summer floes. These lacy leads change shape and size with deformation. One might have expected the big events of deformation to occur where there was some striking lead-like feature, but this was generally not the case. At all large deformations we could see changes in leads, but the leads were usually modest (less than a kilometer)--not those that stood out for their size (2 to 4 km). Some areas which had many leads and looked ripe for deformation moved

We tried to find a measurable feature at least every 2 km in x. In some relatively featureless stretches, this was difficult; in others, we could have found many data points in 2 km. Often one chooses a feature in one image but has difficulty finding its counterpart in the other image. There are two effects. In successive orbits, a moving object is viewed from different angles from which it has a different appearance to the radar. In addition, the ice features in question are at the limit of the resolution and are thus defined by a different grouping of pixels (picture elements) in successive images. Hence, a small feature prominent in one image may be absent in the other or distorted enough to make one uncertain where the cursor should be placed. A somewhat lower magnification than the six power eyepiece in our Bendix plotter would actually help one identify features. On land, features were relatively easy to identify and measure, presumably because the land is stationary and we had chosen to look at nearly identical orbits. With the cursor on an ice feature in one image, our uncertainty in locating the feature in the other image is comparable to the resolution ± 35 m. This error pertains to positioning a bright return in the film image. There is still the question of how closely a bright feature seen in two images corresponds to one particular ice feature. We have not tested this, but the positioning error for ice features can only be greater than that for image features.

OBSERVED DISPLACEMENTS

The 25 km wide strips for the orbits we examined (Figure 1) include 460 km over the Canadian archipelago (x < 0) and 865 km of drifting ice between x = 285 and x = 1150 km. We made no measurements in the near shore region (0 < x < 285) where large displacements carried the ice to the extreme edge or completely out of the second image.

rigidly. Areas which moved approximately rigidly but did show some relative displacement (several hundred meters)--like the noisy segment between x = 385 and x = 435 km--do in fact show many sites at which this deformation could have occurred. This sort of motion seems consistent with an autumn pack with many small floes being consolidated into a winter pack with larger pieces.

ERRORS

Our interest is in the accuracy of relative position (x,y), of displacement (u,v) and of displacement differences $(\Delta u, \Delta v)$. We have

$$
\begin{aligned}
u &= x_a^2 - x_a^1 \\
v &= y_a^2 - y_a^1 \\
\Delta u &= (x_b^2 - x_b^1) - (x_a^2 - x_a^1) \\
\Delta v &= (y_b^2 - y_b^1) - (y_a^2 - y_a^1)
\end{aligned}
\tag{1}
$$

where the subscript identifies the ice particle and the superscript, a time. Discontinuities in displacement occur for only a few unique pairs of adjacent particles.

Systematic errors arise from various sources which we will discuss in turn below. We cannot now eliminate these errors from the data; the discussion is aimed at eliminating them from future measurements of these SAR images. There is a random zero mean error due to the 35 m resolution of the system. Its standard deviation is 35 m in (x,y), $\sqrt{2}$ times this or 50 m in (u,v) and 70 m in $(\Delta u, \Delta v)$. It is seen in Figure 4 as the vertical scatter about the trends.

Along track stretching. The mechanics of the processor can introduce stretching of up to 1% in the along track direction. We have compared our images to maps and find 0.25 to 0.50% stretching. Conservatively then, we take our values of x to have an error of 0.005 x.

When two images are compared, this stretching may add or partially cancel. We find that the image on October 8th is compressed about 0.26% relative to that on the 5th. This is the trend in Figure 4. Since this trend is not necessarily maintained out over the ice, we do not correct the data. If we had fixed land points in the Siberian end of our images, we would probably have enough information to remove or reduce this error. The resulting error in u is roughly -0.0026 x; at the far end of the strip (x = 1150 km) this amounts to 3 km. For displacement differences Δu, the errors in neighboring u's effectively cancel.

Across track drift. Figure 4 shows a nearly constant error in v of -0.0001 x $+0.38$ km. As with u, this error cancels when one calculates Δv for neighboring features. The error in v can arise from several effects, two related to the orbits and the third, to the processor. The two orbits are not quite identical but cross at a slight angle near their tops. This causes an apparent across track displacement which grows with distance from the crossing. The orbital data needed to remove this error are available. The other orbital contribution to this error is made by the practice of taking satellite altitude to be fixed when it actually is slowly changing along the orbit. Enough is known about the actual altitude to remove these errors. Occasionally (perhaps once or twice per orbit) the assumed altitude is corrected, and at these locations along the orbit, there is an apparent jump in the across track position. There were no altitude corrections in the images we studied. Different processor set-ups can introduce an offset in the across track location of the orbit on the order of a few hundred meters. This can only be detected and removed by locating the x-axis with a land point as was done with the y-axis. Again land points at each end of the pass (in the absence of altitude corrections) would remove these sources of error.

Across track distortion. The relation between the slant range (the distance from the satellite to a point x,y on the ground) and the across track coordinate y is non-linear. For convenience it is approximated to be linear, introducing a distortion. The specification for the optically processed data is that this distortion be no more than 3% of the distance from the centerline of a 25 km strip. We have no independent check and so, use this value. The greatest distance from any of our data points to the centerline is 6.6 km, with an error of 0.2 km. The 3% systematic error in y causes a displacement error of 3% of v, and the error in Δv is 3% of Δv. It would be a simple matter to correct all y values for the across track error.

DISCUSSION

Despite some early pessimism about the quality of the SEASAT SAR optical data, from them one can obtain high quality measurements of ice movement. The major errors in our measurements can be removed with more work and information. One needs land in both ends of the ice imagery, orbital parameters (equatorial crossings), altitude data, and the correct relation between the across track coordinate and the slant range.

There is no handicap in working with images which have not been digitally corrected. Coordinates of features can be measured from the slightly distorted images and can be corrected by the same algorithms one would use to correct the whole image, with considerable saving in processing cost and effort. This statement may be as true for pattern recognition and area measurements as it is for displacement measurements. Others have made this point [e.g. *Leberl, et al.,* 1979], but we repeat it here for emphasis.

There are many ways to look at SAR data. Our approach has been limited to making observations along a line. Thus, we have avoided making mosaics and have minimized the problem of mapping different orbits into a common

coordinate system. Neither have we attempted to establish absolute position except for illustrating the orbit in Figure 1. Other researchers attempting a more general treatment will encounter more difficulties than we have. We are convinced though of the usefulness of these data and the pity of SEASAT's early failure.

There are more pairs of congruent strips of SAR data between July and October 1978. Their analysis could be expected to show some dramatic seasonal changes in the velocity field structure, both in the sizes of rigid pieces and in the variance of the motion. There does not seem to be enough data to explore regional differences.

Given that knowledge of ice motion is essential to any study of mass balance, high resolution radars are a promising source of data on an operational level. Their disadvantage is their high data rate. An alternative worth studying is collecting radar data only in a small fraction of the polar oceans in data windows say 30 km in diameter spaced on a 500 km grid. The data set would serve the same purpose as an array of buoys. The details of the motion would not be observed operationally, but their statistics would be known from a few records of the sort reported here.

Bryan, M. L., Interpretation key for SAR (L-band) imagery of sea ice.
Proceedings of the Amer. Soc. of Photogrammetry, p. 406-435, Falls
Church, VA 1976.

Bryan L., T. Farr, F. Leberl and C. Elachi. Synthetic aperture radar imagery
of the AIDJEX triangle. AIDJEX Bulletin No. 37, 161-166, +21 figures, 1977.

Harger, R. O. Synthetic Aperture Radar Systems. Academic Press, New York, 1970.

Jordan, R. L. The SEASAT-A synthetic aperture radar system. J. of Ocean
Engineering, Vol. OE-5, No. 2, p. 154-164, 1980.

Leberl, F., M. L. Bryan, C. Elachi, T. Farr and W. Campbell. Mapping of
sea ice and measurement of its drift using aircraft synthetic aperture
radar images. J. Geophys. Res., 84, No. C4, p. 1827-1835, 1979.

Nye, J. F. The use of ERTS photographs to measure the movement and deformation
of sea ice. J. Glaciol., 15, No. 73, p. 429-436, 1975.

Reeves, R. G., ed. Manual of Remote Sensing. Amer. Soc. of Photogrammetry,
Falls Church, VA 22046, p. 454-466, 1975.

Figure Captions

Figure 1. Approximate ground path of the inboard SAR swath on 2, 5 and 8
October 1978. Solid lines outline the portion of the path where
displacement measurements were made.

Figure 2. Sea ice displacements between 5 and 8 October 1978:
(*upper*) along track displacement vs. along track position,
(*lower*) across track displacement vs. along track position.

Figure 3. Motion of ice pieces from 5 to 8 October 1978. The line segments
represent floes moving rigidly from the lower position to the
upper position. For instance, the segment AB on 5 October moved
to A'B' by 8 October.

Figure 4. Apparent displacement over land from 5 to 8 October 1978. Since
the true displacement is zero, these data represent measurement
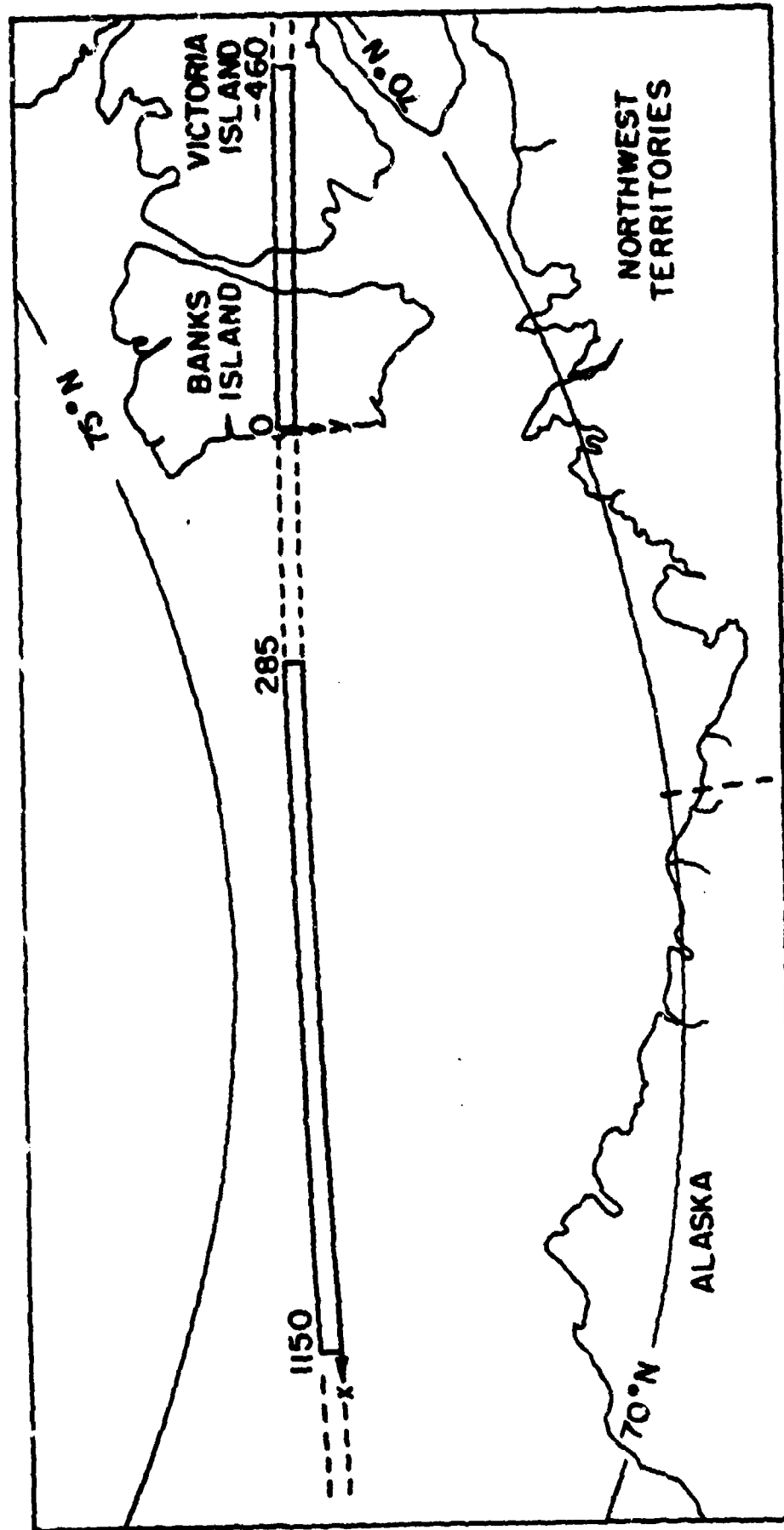errors.

Fig. 1. Approximate ground path of the inboard SAR swath on 2, 5 and 8 October 1978. Solid lines outline the portion of the path where displacement measurements were made.
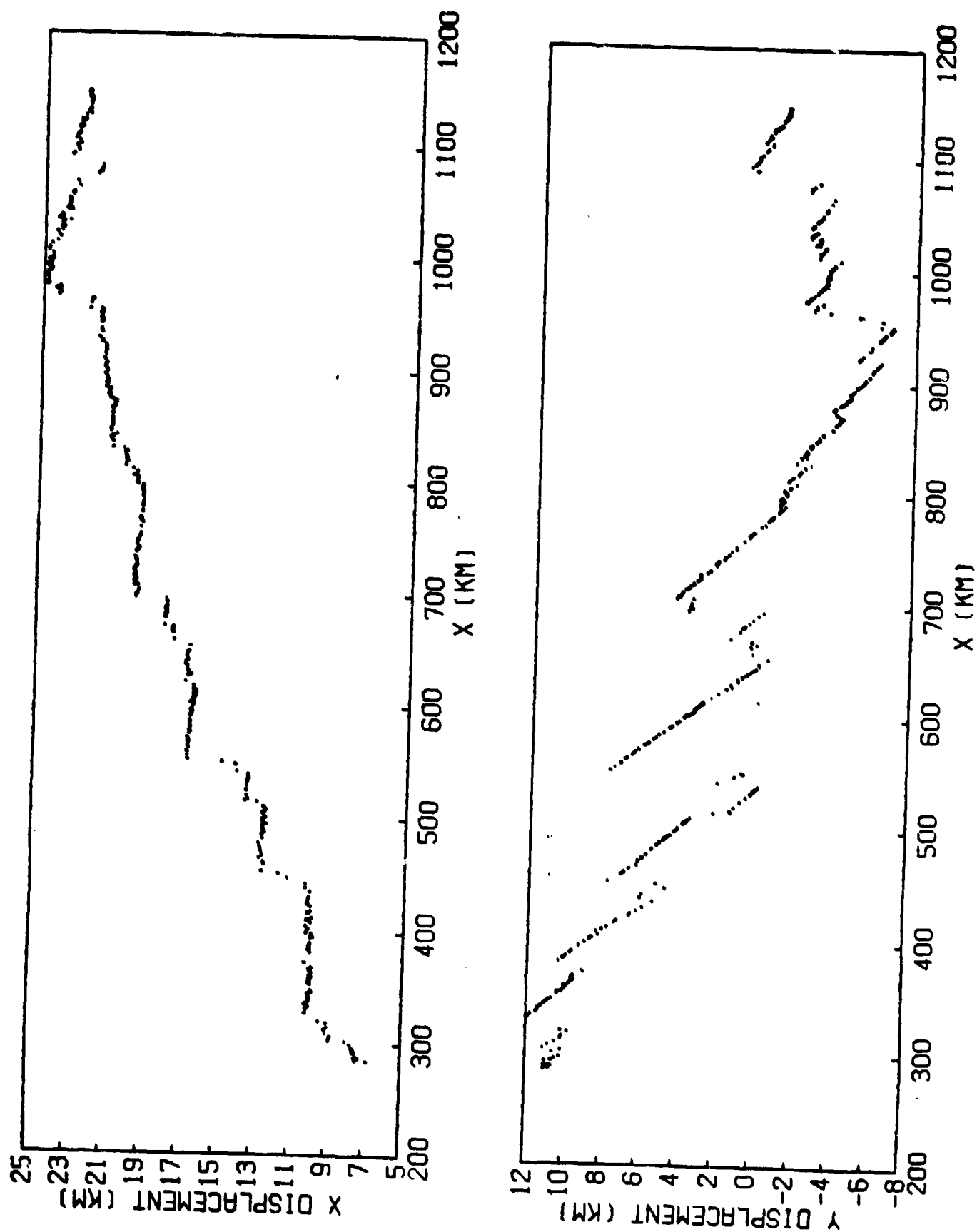
Hall and Rothrock

Fig. 2. Sea ice displacements between 5 and 8 October 1978: (*upper*) along track displacement vs. along track position. (*lower*) across track displacement vs. along track position.
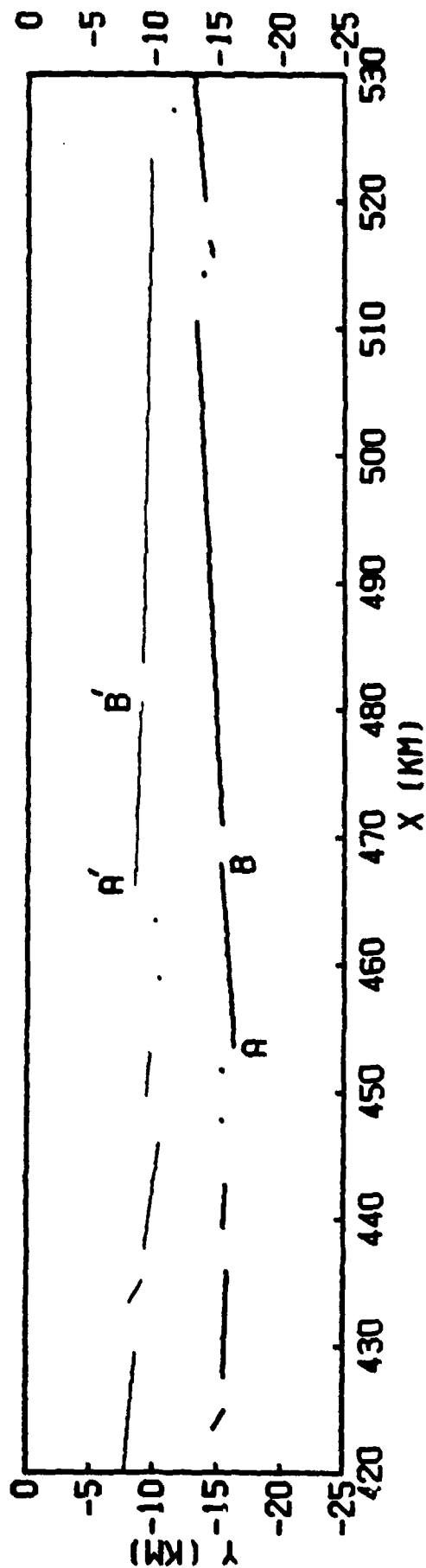
Hall and Rothrock

Fig. 3. Motion of ice pieces from 5 to 8 October 1978. The line segments represent floes moving rigidly from the lower position to the upper position. For instance, the segment AB on 5 October moved to A'B' by 8 Uctober.

Hall and Rothrock

Fig. 4. Apparent displacement over land from 5 to 8 October 1978. Since the true displacement is zero, these data represent measurement errors.

Hall and Rothrock

APPENDIX B

KINEMATICS OF SEA ICE

by Alan S. Thorndike

CHAPTER 5. KINEMATICS OF SEA ICE   A. S. Thorndike

Contents   Page

Miscellaneous: Acknowledgments, References, Figure legends, Figures, Tables

List of Figures

Kinematics is that branch of physical science dealing with motion
itself and not with the causes of the motion. Attention is focused, in
this chapter, on how sea ice moves. The deeper question of why sea ice
moves as it does is addressed in the following chapter on sea ice dynamics.
For some scientific and practical applications, knowledge of the ice kine-
matics (as opposed to the dynamics) is sufficient. As examples, consider
gouging of the sea floor in shallow water, the transport of natural debris
or pollutants, the impact loads on structures, navigability in icy regions,
and the movement of the ice edge. Aside from these applications, the study
of kinematics is a basic step toward understanding the dynamics.

Figure 1 illustrates the idea that the motion of sea ice is the response
of the ice pack to external forces. To understand the response of the ice
one needs to monitor both the driving forces and the motion. Since we will
discuss only the motion here, there will be the underlying ambiguity of
whether the results inform about properties of the ice itself or about the
driving forces. We will see for example that the ice motion is nearly non-
divergent. But we should not conclude on this basis alone that the ice is
an incompressible material. The correct explanation could be that the net
driving force is itself nearly non-divergent. Because of this ambiguity
in the interpretation of kinematic data, it is useful to think of the study
of the kinematics as part and parcel of the broader study of sea ice dynamics.

The fundamental kinematic notion is that all pieces of ice have an
identity which is preserved in time. If we identify a piece of ice say by
making a small mark on the ice surface at position X at time o , the assumption
is that at some later time t , the piece of ice as identified by that mark will
be at a position x . This defines the position function $x(t,X)$ with $x(o,X)=X$.
We do not mean to imply by this that ice floes retain their identity indefi-
nitely, only that it is possible to track individual points. Two points
originating on the same ice floe may very well wander apart in time, but we
assume we could keep track of them.

There are difficulties with the notion of a position function. It is
natural to consider the space domain to be the two dimensional surface of
the Arctic Ocean, say $\underline{X}$. At $t=o$ there will generally be some points in $\underline{X}$
which are not covered by ice, so $x(t,X)$ is not defined for some $X \epsilon \underline{X}$.

Further, ice is always being created and destroyed thermodynamically, so the position function $x(t,X)$ is only defined for an interval of time.

Finally, the idea that the small mark retains its identity is questionable. This is a common problem in the definition of the motion of a turbulent fluid. After a time the marked fluid has mixed with the unmarked and it is no longer possible to assign a position to the mark. Something of the same sort happens with sea ice. Despite these shortcomings, the notion of a position function is the best we have. Furthermore this notion corresponds exactly with most of the observations we have. We will use the term trajectory for the function $x(t,X)$ where X is held constant. The initial position X serves to label ice particles and we refer to the trajectory $x(t,X)$ of the particle

redundant?

5.1 Observations

The most common observations of ice motion are of trajectories of ice particles consisting of a sequence of measurements (z_i, t_i), $i = 1, \cdots N$ where

$$z_i = x(t_i, X) + \varepsilon_i$$

The measurement error is represented by ε_i.

In passing we mention that other kinds of measurements of ice motion have been made. Hunkins (1967) and McPhee (1978) for instance inferred the ice velocity using current meters suspended from the ice into what they assumed to be essentially a static ocean. These data were used to study motion on the time scales of hours. An attempt to study motions on much shorter time scales using accelerometers was made by Craig (1972).

Many techniques have been used to measure ice trajectories. These are summarized in Table I. Each technique has its good and bad features. Over the past decade most data have been obtained by satellite positioning which works somewhat as follows. Suppose a stable frequency f_0 is transmitted by a device on the ice. The signal received at the rapidly moving satellite will have a frequency f which has been shifted by the Doppler effect: $f = f_0 + \Delta f$. The Doppler shift Δf is related to the rate of change of distance between the device on the ice and the satellite $\Delta f \sim \frac{d}{dt} |x_{sat} - x_{ice}|$. The received frequency f is measured at several times. If the satellite coordinates are known at these times, then each measurement produces an equation with unknowns f_0 and x_{ice}. Generally several measurements are made during the 10 to 20 minutes it takes for the

TABLE I

technique	basic measurement	sampling rate	accuracy	comments
Hunkins et al, 1971 celestial navigation	azimuth and elevation of heavenly bodies	1 per day	10^3 m	weather dependent
Martin et al, 1978 satellite navigation	Doppler shift of stable transmitted signal	30 per day	30–500 m	
Thorndike, 1973 acoustic tracking	travel time from ice to fixed reference on the ocean floor	up to 1 per minute	5 m	limited range, elaborate instrumentation, relative position only
Tucker et al., 1980 Tabata et al., 1980 radar	travel time from source on shore to target on ice	no limit	< 1 m	limited to near shore
Hall, 1980 Landsat imagery	location of identifiable ice features	erratic	80 m	weather dependent, good space resolution, poor time resolution
Hall & Rothrock, 1981 synthetic aperture radar imagery (SEASAT)	location of identifiable ice features	1 per 3 days	80 m	no system available at present, properties of future systems unclear

B-2a

satellite to pass by. The several equations are solved simultaneously for f_0 and x_{ice}. Precise positioning requires a stable transmit frequency, precise measurement of the received frequency, and precise knowledge of the satellite coordinates. With care, errors can be controlled to the order of tens of meters, as in the best uses of the Navy Navigation Satellite System.

Satellite systems which serve primarily to relay data from automatic data platforms (or buoys) to data processing centers also determine the location of the transmitting data platform, using the same Doppler positioning principle. The ARGOS system currently on the NOAA-B satellite can relay data from up to 30 sensors and determine platform locations to an accuracy of a few hundred meters about ten times per day. Fully automatic platforms cost in the neighborhood of $6,000 with additional costs depending on the desired sensors.

Satellite imaging systems can also be used to measure ice motions, provided that some features on the ice can be identified in a sequence of images. Because of their all season and all weather capability and good resolution, imaging radar systems will probably be best. The basic angular resolution of these systems is approximately the ratio of the wavelength of the radar signal to the diameter of the antenna. To achieve an angular resolution of 10^{-5} (10 meters at a range of 1,000 kilometers) with a wavelength of 25 cm (1.2 GHz) requires an antenna 25 km in diameter. Although such large antennas cannot be constructed in space, it is possible to synthesize large antennas by using data from several points along the satellite's orbit. The determinations of the geographical position of an ice feature with the SEASAT data contained errors of up to 3 kilometers (see Hall and Rothrock, 1981). Unless these errors can be reduced the data are not particularly valuable for measuring the displacements over intervals of a few days or less. However, the errors are highly correlated in space and are essentially eliminated in estimates of the spatial variability of the ice motion.

The attractive feature of imaging radar systems is their potential to sample densely in space. Hall and Rothrock's work suggests that it will be possible to track roughly one feature per square kilometer, which will resolve most of the spatial structure of the field of motion. Techniques for extracting data from the images or from the raw data are still rather primitive. No doubt satisfactory automated techniques for identifying and tracking features will be developed when the need arises. At present there is no imaging radar system in space. Planning is underway for a system to be in operation perhaps by 1985.

5.1.1. Sources of data

The earliest ice motion data are the trajectories of ships beset in the ice. These are followed by the trajectories of numerous Soviet and U.S. drifting research stations, and more recently by the trajectories of automatic data buoys. The following list of data sources is by no means complete.

Experiment	Reference	Description
T-3	Hunkins et al., 1971	Monthly positions May 1962-December 1970
Beset ships and drifting stations before 1970	Hastings, 1971	A chart showing most prior trajectories, one point per month; includes: Fram, Jeanette, Maud, Sadko, Sedov, Tegetthoff, British Trans-arctic Exp., Alpha, Arlis I, Arlis II, Charlie, North Pole 1-20, T-3.
AIDJEX 1972	AIDJEX Staff, 1972	100 km triangle, Beaufort Sea, March and April 1972.
AIDJEX 1975-76	Thorndike and Cheung, 1977	Manned camp positions and velocities tabulated at 6 hr intervals, daily buoy positions.
1976-77 buoys	Thorndike and Cheung, 1977	Tabulated daily positions of Beaufort Sea buoys.
1979 buoys	Thorndike and Colony, 1980	Tabulated daily positions, 25 buoys, analyses of surface pressure plotted daily.
1980 buoys	Thorndike and Colony, 1981	As above.
Fram I, 1979	Hunkins et al., 1979	March-May 1979; 84°N, 9°W
LOREX 79	Popelar et al., 1981	Three stations, 100 km spacing April, May 1979; 88°-90°N.

5.2 The general circulation

The main features of the long term circulation, Figure 2, are the clockwise circulation in the Beaufort Sea—and the motion of ice from the Siberian coasts across the North Pole and through the Greenland-Spitsbergen passage. Time honored nomenclature for these features are the Beaufort Gyre and the Transpolar Drift Stream. Some handy numbers for these long term features are:

center of Beaufort Gyre: 80°N, 155°W, half way between Pt. Barrow, Alaska and the North Pole

time to make 1 circuit: 5 years

time to traverse Transpolar Drift Stream: 3 years

area flux through Greenland-Spitsbergen Passage:
300 km^2/day or about 20% of the area of the basin per year.

This pattern of motion exists only as an average over several years. On shorter time scales there are departures from the long term pattern. Consider for example the trajectories plotted in figure 3 for the year 1979 and figure 4 for 1980. The trajectories are characteristically meandering and convoluted showing that on daily and monthly time scales the ice motion differs markedly from the long term mean. Notice the major anomaly which occurred in the summer of 1980 when the motion of several buoys for several months was in the opposite sense from the long term mean. These departures of the actual motion from the long term pattern in most cases represent the response of the ice to the passage of atmospheric systems.

If we ignore the forces and examine only the ice motion, the departures from the mean circulation appear aperiodic and chaotic. The departures can be thought of as random but they are not without structure. Our objective now is to clarify this structure.

5.3 Ice velocity

The ice velocity field can be defined by the relationship

$$u(x,t) = \lim_{h \to 0} \frac{x(t+h,X) - x(t,X)}{h} .$$

Here the particle label X plays no role.

This definition is meaningful only if the limit exists. From a practical point of view it is useful only if the limit exists _and_ is approached when the interval h decreases to the time interval τ between observations.

In figure 5 several sets of observations of ice motion are plotted, showing the variation of one coordinate of position versus time. Successive data sets divide the sampling interval τ by 15 and improve space resolution by the same factor, giving a sequence of closer and closer perspectives on the motion. By constructing velocity estimates, $u_k(t) = [x(t+k\tau,X) - x(t,X)]/k\tau$ for k decreasing to 1, one can examine the limiting process. In the first two figures of the sequence, u_k continues to change appreciably for small k . In the last two figures, $u_k(t)$ at most times t becomes almost independent of k for small k , implying that on these time scales, $\tau \leq 15$ minutes, the ice indeed possesses a velocity.

Convergence of $[x(t+\tau,X) - x(t,X)]/\tau$ to a definite limit implies that the increment $x(t+\tau,X) - x(t,X)$ *is* proportional to τ for small τ. For random processes, a useful condition for convergence is mean squared convergence in which the <u>variance</u> of the increment becomes proportional to τ^2 for small τ. This can be readily tested for ice trajectories by plotting $E(x(t+\tau,X) - x(t,X))^2$ versus τ on a log-log plot, as is done in figure 6. The process is differentiable if the graph has slope of 2 for small τ.

From a practical point of view the process ceases to be differentiable at measuremen intervals τ for which the slope of the graph departs appreciably from 2. The evidence in figures 5 and 6 implies that the ice does have a velocity and that it can be resolved with a sampling interval of about three hours.

Time averaged velocities can be defined without reference to the limiting process. Let $u(t,T,x)$ be the time averaged velocity at t.

$$u(t,T,x) = \frac{1}{T}\left[x(t+T_2,X) - x(t-T_2,X)\right] = \frac{1}{T}\int_{t-T/2}^{t+T/2} u(s,x)\,ds \ .$$

This quantity $u(t,T,x)$ and its properties depend on the duration T of the time averaging. For example, the variance of $u(t,T,x)$ will in general be less than the variance of $u(t,x)$ because the T average has suppressed contributions to the variance on shorter time scales. Also, from a dynamical point of view, the equations which $u(t,T,x)$ satisfies should involve T as a parameter. Different physical processes may be responsible for determining $u(t,T,x)$ for different values of T.

Typical ice velocities range from 0 to 20 cm sec^{-1}. An extreme velocity of 140 cm sec^{-1} has been observed. Two histograms of ice speed are shown in figure 7 , one corresponding to a full year of observations, the other restricted to summer observations. The winter data contained several periods of essentially zero motion. During the summer the ice was never observed to stop.

In the following pages particular importance is attached to the time and space variability of the ice motion. We will often refer to the variance of velocity, $E((u-\bar{u})^2 + (v-\bar{v})^2) = \phi^2$. This quantity has been evaluated from many observations; it varies appreciably with season and with location. Table II gives estimates of the velocity variance for each of the buoys shown in figure 3.

TABLE II

1979 data, 1 point per day

Buoy ID	velocity variance	number of data points
1901	59 $cm^2 sec^{-2}$	342
1902	48	295
1903	50	284
1905	210	231
1906	81	299
1907	37	229
1908	174	61
1909	38	267
1911	19	62
1913	84	314
1914	83	282
1915	172	31
1916	57	172
1918	35	283
1917	29	219
1920	54	293
1923	63	302
1924	167	72
1925	67	280
1926	168	59
1927	62	311

5.3.1 Velocity time series

The ice velocities deduced from trajectories should be interpreted from the Lagrangian point of view since the measurements are made following the material particle. If many trajectories are measured simultaneously it is possible to obtain by interpolation velocity time series at fixed Eulerian points. Although the Lagrangian description is more directly measurable, it has the drawback of sampling both the time and space variations in velocity. The differences between the Lagrangian and Eulerian points of view is not of great practical importance in the motion of sea ice. This is because most of the variability in the ice motion is driven by the wind, and the space patterns in the wind field move across the basin so much faster than the ice moves, that all points, Lagrangian or Eulerian, experience essentially identical stochastic forcing. Consequently, Lagrangian and Eulerian time series of sea ice velocities look just about the same.

A typical velocity time series, taken from an ice station trajectory, say, will have a mean velocity usually less than 3 cm sec^{-1}, and it may show a trend. When these effects are removed from the time series what remains are the fluctuations with time scales longer than the sampling interval and shorter than the length of record $\mathcal{T}$. The AIDJEX position data for instance, serve to resolve fluctuations on time scales from a few hours up to a few months, ($\gamma \approx$ 1 hour, $\mathcal{T} \approx$ 1 year). Over this range of time scales the ice velocity has a power spectral density as sketched in figure 8.

The power spectral density is plotted for positive and negative frequencies corresponding to counter-clockwise and clockwise rotations of the velocity vector. At the end of this section an algorithm is given for calculating the spectra of vector time series. We interpret the velocity vector time series $u(t, x)$ as a complex time series with the Fourier decomposition

$$u(t,x) = \int_{-\infty}^{\infty} a(\omega) \, e^{i\omega t} \, dt \; .$$

The power spectral density is the real function $S(\omega) = a(\omega) \, a^{*}(\omega)$, defined in the frequency range $-\frac{1}{2\gamma} < \omega < \frac{1}{2\gamma}$.

The integral of the spectral density over this frequency range is the variance ρ^2, and the integral over any frequency band is the part

B - 7

of the total variance contributed by fluctuations with frequencies in that band. A useful way to summarize the information contained in the spectrum is to state the fraction of the total variance coming from frequencies greater than a certain value. We find:

Table III Fraction of total variance from frequencies exceeding

frequency:	1 cycle per month	2	4	15	30	60
period:	1 month	2 weeks	1 week	2 days	1 day	12 hours
	58%	45%	34%	12%	7%	3%

The equation of motion for sea ice balances the ice acceleration against air stress, water stress, pressure gradient forces due to the sloping sea surface, and internal ice stress gradients. While it is not the purpose here to examine the ice dynamics, it is useful to relate features of the ice velocity spectrum to these driving forces. In the central basin about 75% of the variance of the ice velocity can be explained by the local geostrophic wind (Thorndike and Colony, 1981). In fact, the ice velocity fluctuations are roughly proportional to the local wind fluctuations. This implies that the spectra of the ice velocity and of the wind should have approximately the same shapes (see figure 7).

The water stress depends on the difference in velocity between the ice and the upper ocean. If the ocean is at rest the water stress is simply a drag opposing the ice velocity and its only effect is to reduce the ice response near the inertial frequency.———————————————————— —— ——
If the ocean is in motion, the ice will be carried along with it, and should acquire spectral traits similar to those of the ocean. Unfortunately the spectral signature of motion in the Arctic Ocean is poorly known. The long term circulation of the upper ocean appears to be similar to that of the ice, with a clockwise circulation in the Beaufort Sea and a transpolar current flowing from Siberia through the Greenland-Spitsbergen passage. It probably is not productive to ask whether the ice drives the long term ocean circulation or vice versa because, in the long term, the ice should be thought of as part of the upper ocean. In any case the long term ocean behavior does not affect the spectrum we are considering since we have subtracted out the long term mean velocity.

Fluctuations in ocean currents on shorter time scales have been observed but it is not yet possible to say how great their effect on the ice velocity may be. Briefly they are:

1. Monthly variations are apparent in the currents deduced from wind and ice motion observations by Thorndike and Colony, 1981.

2. Manley's (1981) study of subsurface eddies during AIDJEX described numerous features with velocities of about 50 cm sec^{-1}, a length scale of 10 kilometers, and a depth of 50-200 meters. He found no expression of these structures in the ice motion.

3. **Inertial oscillations.** The balance between the ice acceleration and the Coriolis force leads to oscillatory ice motion with a period which varies from 12.77 hours at 70°N to 12 hours at 90°N. Inertial motions are always clockwise—hence the negative value for the frequency—in the Northern Hemisphere because the Coriolis force always accelerates the velocity to the right. Inertial motions in sea ice were first described by Hunkins (1967) and have received subsequent study by McPhee (1979) and Colony and Thorndike (1980). The amplitudes can reach 0.20 m sec^{-1} during summer when the ice pack is comparatively loose. Their effect on the summer ice velocity spectrum is striking (see figure 10).

4. **Tides.** Tidal currents in the central basin are small because of the great depth. Theoretical estimates are in the range of 1-2 cm sec^{-1}. Over the shallow continental shelves the amplitudes are predicted to be at least an order of magnitude greater (Kowalik and Untersteiner, 1978). These theoretical estimates are for the lunar semi-diurnal tide. Evidence from tide gauges around the basin summarized by Sverdrup (1926) imply that the lunar semi-diurnal (period 12.47 hr) and the solar semi-diurnal (12 hr) tides are the dominant tidal constituents in the Arctic Ocean.

The prediction of a large amplitude of the tidal current over the shelf is confirmed by Sverdrup's observations from the <u>Maud</u>; Nansen may also have observed tidal motion in the ice pack surrounding the <u>Fram</u>. Because the tidal and inertial periods are so close it may be difficult to diagnose observed motions correctly. Nevertheless there are several differences between the two kinds of motions which can sometimes be used to distinguish them. First the tidal vector traces out an ellipse during one period. An ellipse can be viewed as the sum of a clockwise circle and counter-clockwise circle. Thus, unless the tidal ellipse should happen to be exactly a clockwise circle, it should have some expression on the counter-clockwise

side of the spectrum. Inertial motion is strictly clockwise. Second, at a fixed point, tidal motions should have a fixed phase. Inertial motion on tne other hand, acquires a new phase every time the ice receives a sudden impulse of momentum. Third, the phase of tidal motion should vary smoothly and slowly in space. Inertial motions at different points may have no fixed phase relationships.

The motion described by Sverdrup can hardly be mistaken for inertial motion. The smooth variations in phase as the Maud moved from Wrangel Island to the New Siberian Islands, and the clearly elliptical cycle described by the measured velocity vector are not compatible with inertial motions.

Most ice trajectories which have been analyzed in the western literature have been over the deep basin where the tidal motion is small. Careful observations and analysis would be required to detect a tid... component of order 1 cm sec^{-1} since it would be mixed with an inertial component which is often much larger and with a rich spectrum of other types of motions.

The Soviet literature contains many references to tidal motion in sea ice. Doronin and Khiesin (1977) and Zubov (1943) each devote several pages to the subject.

An important consequence of the tidal motion is the associated cycle of convergence and divergence caused by the difference in phase of the tidal cycle at different points. Periodic opening and closing of the ice in the shallow seas has an effect on the heat exchange between the atmosphere and the ocean and on the rate of ice production. The theoretical calculations of Kowalik and Untersteiner indicate maximum divergence rates in the shallow seas exceeding 10^{-6}sec^{-1} which is enough to produce one percent opening during the tidal cycle. Their theoretical estimates of the divergence rate associated with tides over the deep ocean are three orders of magnitude smaller.

Calculation of cross power spectral density for two two-dimensional vector time series.

Given: two discrete complex time series u_i, V_i, $i = 1, ..., N$ with sampling interval τ.

Step 1. Select M, the number of lags.

Step 2. Remove the mean and trend from each time series.

Step 3. Compute cross covariances

$$\xi = \begin{cases} \frac{1}{N} \sum_{j=1}^{N-\ell} u_{j+\ell} V_j^* & \ell = 0, 1, ..., M, \\ \frac{1}{N} \sum_{j=1-\ell}^{N} u_{j+\ell} V_j^* & \ell = -M, -M+1, ..., -2, -1 . \end{cases}$$

B-10

Step 4. Define spectral window

$$w_\ell = \frac{1}{2}\left(1 + \cos\frac{\pi\ell}{M+1}\right) \qquad \ell = -M, \cdots, M.$$

Step 5. Calculate spectrum S and frequency ω

$$S_k = \tau \sum_{\ell=-M}^{M} w_\ell \, r_\ell \, e^{-2\pi\ell k \sqrt{-1}}$$

$$k = -M, \cdots, M.$$

$$\omega_k = \frac{k}{2M\tau}$$

5.3.2 Velocity correlations in time.

An alternative characterization of a random function is its autocorrelation function. The discussion in the previous section of the power spectral density of the time function $u(t)$ at a fixed or moving point could have been given in terms of the autocorrelation function

$$R(\tau) = \frac{E\, u(t+\tau)\, u^*(t)}{E\, u(t)\, u^*(t)} = \frac{1}{q^2}\, E\, u(t+\tau)\, u^*(t).$$

The two functions $S(\omega)$ and $R(\tau)$ are Fourier transforms of each other and therefore contain equivalent information. Which description is the more useful depends on the application. The spectrum is useful for distinguishing physical processes with distinct characteristic frequencies; for example separating the free inertial oscillations from the wind forced motion. On the other hand the autocorrelation function is more useful for questions related to prediction or experiment design. For example the question: "How well can tomorrow's ice velocity be predicted on the basis of today's velocity," has an answer involving the autocorrelation function $R(\tau)$ evaluated at $\tau = 1$ day.

The autocorrelation function is complex. Its real part contains information about the lagged correlations of the x component of velocity with itself

and the y component with itself. The imaginary part has information about the lagged correlations between the x and y velocity components. If the velocity of a piece of ice undergoing an inertial oscillation has a positive x component at a certain time, it will have a negative y component three hours later. The imaginary part of the correlation should have negative peaks at 3 hours, 15 hours, etc.

The autocorrelation function for the velocity time series at the AIDJEX ice station Caribou is shown in figure 11. The autocorrelation function estimated by the 1979 buoy data for the central basin is shown in figure 12. The real part of the correlation falls to about 0.7 after one day, 0.4 after two days, and decreases slowly at longer lags. The large correlation at lag one day indicates that persistence (the forecast strategy which predicts that the future will be the same as the present) will have some skill for one day forecasts.

As expected the autocorrelation from Caribou has negative peaks in the imaginary part at 3 hours, 15 hours, etc. Generally though the imaginary part is small. If the inertial motions are not of interest in a particular application, the imaginary part of the autocorrelation function can safely be ignored. This is equivalent to treating the two velocity components as independent time series.

5.3.2.1 Application of the time autocorrelation function.

It is desired to estimate the ice velocity u at time t given observations z_j at times t_j, $j = 1, \cdots, N$. Suppose the observations have zero mean random errors $\varepsilon_j = z_j - u(t_j)$ which have covariance

$$E \varepsilon_j \varepsilon_k^* = \sigma^2 \delta_{jk} .$$

The delta function expresses the independence of errors at different times. Finally suppose the errors are independent of the actual velocities. Choose an estimator $\hat{u}$ which is a linear sum of the observations.

$$\hat{u} = \sum_{j=1}^{N} \alpha_j z_j$$

It is desired to find the complex constants α_j which give the best estimate $\hat{u}$ in the sense that $F(\alpha_1, \cdots, \alpha_N) = E(\hat{u} - u)(\hat{u} - u)^*$ is minimized. This is accomplished by differentiating F with respect to the real and imaginary

parts of each α_j and equating to zero. The result is the system of complex equations for the unknowns $\alpha_1, \cdots, \alpha_N$:

$$\sum_j \alpha_j E z_j z_l^* = \left(E z_l u^* \right)^*$$

A further reduction is achieved by noting that

$$E z_j z_l^* = E u_j u_l^* + \sigma^2 \delta_{jl} \quad \text{and} \quad E z_l u^* = E u_l u^* \quad .$$

Use of the matrix notation $Z = \{z_j\}$, $A = \{\alpha_j\}$, $M = \{E z_j z_l^*\}$, $P = \{E z_l u^*\}$ gives the compact expressions

$$\hat{u} = A^T Z \quad \text{and} \tag{1}$$

$$M^* A = P \quad .$$

Furthermore the estimation error is

$$F = q^2 - P^T M^{-1^T} P^* \quad . \tag{2}$$

With these two expressions we can answer a number of practical problems.
1.   What sampling rate is required to insure good two point interpolation in time? For given sampling interval τ and measurement error variance σ^2, we write eq. 1 as

$$\begin{pmatrix} q^2 + \sigma^2 & q^2 R(\tau)^* \\ q^2 R(-\tau)^* & q^2 + \sigma^2 \end{pmatrix} \begin{pmatrix} \alpha_1 \\ \alpha_2 \end{pmatrix} = \begin{pmatrix} q^2 R\left(\frac{\tau}{2}\right)^* \\ q^2 R\left(-\frac{\tau}{2}\right)^* \end{pmatrix}$$

The solutions for the α_j , which in this case are complex conjugates for reasons of symmetry, and for F are sketched in figure 15. The solution technique extends trivially to interpolation involving more points.

The optimal choice of the weights α_1 and α_2 is not $\alpha_1 = \alpha_2 = \frac{1}{2}$. This linear interpolation between the two data points is the most natural scheme, and it is quite good for small τ , and small σ^2/q^2 , but it is not the optimal interpolation. Especially at large τ , a smaller error variance is achieved by giving less weight to the observations. For very large τ the optimal estimate is simply $\hat{u} = 0$, $(\alpha_1 = \alpha_2 = 0)$ since, in this case the two observations are so removed in time as to have no correlation with the desired velocity.

The measurement error σ affects α_j and F slightly. The dependence of F on the sampling interval τ is quite strong. It appears that if one needs to know each velocity component to ± 3 cm sec^{-1} , $F = F \, \epsilon_u^2 + \epsilon_v^2 = 18$ cm sec^{-1}, a sampling interval of about six hours is required even with perfect measurements.

2.   What errors are expected in forecasts based only on the present velocity? Here we obtain

$$\alpha = \frac{R(\tau)^+}{1 + \sigma^2/q^2}$$

$$\tag{2}$$

$$F/q^2 = 1 - \frac{R(\tau) \, R(\tau)^+}{1 + \sigma^2/q^2}$$

The forecast skill is plotted for several values of initial error in figure 14.

The prediction error grows with time, approaching the velocity variance q^2 for large τ . From the sketch we see that an optimal 3 hour forecast captures about 75% of the velocity variance, an optimal one day forecast captures about 35% of the variance.

The velocity was assumed to have zero mean in this analysis and in constructing the autocorrelation function (figures 11,12) the long term mean was first removed from the data. In an actual application to a region where the mean is known the best forecast would be

$$\hat{u} = \bar{u} + \alpha (\bar{z} - \bar{u}) \, .$$

Note that the best forecast is not simple persistence ($\alpha = 1$). For long forecasts, the best estimate is the mean$_A$, as equation $\underset{(\alpha=0)}{3}$ correctly indicates.

5.3.2.1. Acceleration

The time autocorrelation function for velocity, figures 11 and 12, behave like $1 - \tau/c$ for small τ . This implies that the velocity is not time differentiable in the mean square sense. Attempts to measure accelerations precisely by sampling over shorter and shorter time intervals may merely result in larger and larger estimates of acceleration. Of course, time averaged accelerations exist and have finite variance.

$$\sigma_a^2 = \text{var} \left\{ \frac{1}{T} \left[u(t+T) - u(t) \right] \right\} = \frac{2q^2}{T^2} \left(1 - R(T) \right)$$

which for small T is $2q^2/cT$ with $c \approx 10^5 \text{sec}$.

It is frequently claimed that the inertial forces due to acceleration of the ice are small compared to other forces acting on the ice. To support this claim a typical average acceleration σ_a is compared for instance, to a typical value of the Coriolis acceleration $f\sigma_u \approx 10^{-4} sec^{-1} \cdot 10\, cm\, sec^{-1}$. Using the above estimate for σ_a , and taking $q^2 = 100\, cm^2 sec^{-2}$, we find $\sigma_a < f\sigma_u$ provided $T > 2\times10^3\, sec$. Thus, roughly a half hour time average is required to bring the acceleration down to the level of other terms in tne momentum balance.

5.3.3 Velocity correlations in space

In earlier sections the emphasis has been on the structure of the complex function u of the real argument t , at a fixed or moving point. In this section, the emphasis is on u as a function of position for fixed time. Certain results are more easily expressed if u and x are regarded as two dimensional vectors rather than as complex numbers. The autocorrelation function

$$q^2\, R(\underset{\sim}{x}_1,\underset{\sim}{x}_2) = E\, \underset{\sim}{u}(\underset{\sim}{x}_1)\, \underset{\sim}{u}^T(\underset{\sim}{x}_2) = \begin{pmatrix} E\, u(\underset{\sim}{x}_1)u(\underset{\sim}{x}_2) & E\, u(\underset{\sim}{x}_1)v(\underset{\sim}{x}_2) \\ E\, u(\underset{\sim}{x}_1)v(\underset{\sim}{x}_1) & E\, v(\underset{\sim}{x}_1)v(\underset{\sim}{x}_2) \end{pmatrix}$$

is a 2 x 2 matrix involving possibly four different functions, whereas the time autocorrelation function involves just two.

The structure of the spatial autocorrelation matrix for sea ice velocities reveals some of the properties of the velocity field. To establish the basic ideas we first determine the structure of the autocorrelation matrix for a homogeneous, isotropic, two dimensional velocity field, borrowing from Kolmogroff's (1941) classic discussion of three dimensional turbulence.

A random field is said to be homogeneous if its statistical properties are invariant under a translation of coordinates, and isotropic if they are invariant under rotations and reflections of coordinates. In particular the autocorrelation matrix for a homegeneous isotropic field must satisfy

$$R(\underset{\sim}{x}_1,\underset{\sim}{x}_2) = R(\underset{\sim}{x}_1+\underset{\sim}{a},\underset{\sim}{x}_2+\underset{\sim}{a})$$ for any $\underset{\sim}{a}$, and

$$q^2 R(\underset{\sim}{x}_1,\underset{\sim}{x}_2) = E\, u(\underset{\sim}{x}_1)\underset{\sim}{u}^T(\underset{\sim}{x}_2) = E\, M\underset{\sim}{u}(M\underset{\sim}{x}_1)[M\underset{\sim}{u}(M\underset{\sim}{x}_2)]^T$$

for any orthonormal matrix M . Multiplication by an orthonormal matrix

accomplishes an arbitrary rotation or reflection of coordinates. Note that the change of coordinates is applied to both the position and the velocity vectors. These definitions make precise the notions that the statistics do not depend on position or direction. By choosing the translation vector $\underset{\sim}{a}$ or the rotation and reflection matrix M suitably, we can see how these definitions of homogeneity and isotropy constrain the form of the autocorrelation matrix.

First, $R(\underset{\sim}{x_1}, \underset{\sim}{x_2})$ depends only on the vector difference $\underset{\sim}{x_2} - \underset{\sim}{x_1}$. To see this, take $\underset{\sim}{a} = -\underset{\sim}{x_1}$. Note that this does not imply that R depends only on the distance $\| \underset{\sim}{x_2} - \underset{\sim}{x_1} \|$.

Second, R is symmetric. This requires using $\underset{\sim}{a} = -\underset{\sim}{x_1}$, $M = -I$ and $\underset{\sim}{a} = \underset{\sim}{x_2}$, to obtain this sequence of equalities:

$$E\, u(\underset{\sim}{x_1}) v(\underset{\sim}{x_2}) = E\, u(\underset{\sim}{0}) v(\underset{\sim}{x_2} - \underset{\sim}{x_1}) = E\left(-u(-\underset{\sim}{0})\right)\left(-v(\underset{\sim}{x_1} - \underset{\sim}{x_2})\right) = E\, u(\underset{\sim}{x_2}) v(\underset{\sim}{x_1}).$$

Third, $E\, u(0,0) v(x,0) = 0$. Here use the reflection invariance in the definition of isotropy by taking

$$M = \begin{pmatrix} 1 & 0 \\ 0 & -1 \end{pmatrix}$$

which changes the sign of the y axis. Then

$$E\, u(0,0) v(x,0) = E\, u(0,-0)\left[-v(x,-0)\right] = -E\, u(0,0) v(x,0)$$

which is only true when $E\, u(0,0) v(x,0) = 0$.

Consequently the autocorrelation function evaluated at $x_1 = (0,0)$, $x_2 = (\tau, 0)$ has the form

$$R\left((0,0),(\tau,0)\right) = \frac{1}{q^2} \begin{pmatrix} E\, u(0,0) u(\tau,0) & 0 \\ 0 & E\, v(0,0) v(\tau,0) \end{pmatrix} = \begin{pmatrix} \beta_{\|}(\tau) & 0 \\ 0 & \beta_{\perp}(\tau) \end{pmatrix} = \mathbb{B}(\tau)$$

involving only two function of distance. $\beta_{\|}(\tau)$ is the correlation between the components of velocity parallel to the line joining two points separated by a distance τ. $\beta_{\perp}(\tau)$ is the correlation between the components of velocity perpendicular to that line.

More generally if $\underset{\sim}{x_1}$ and $\underset{\sim}{x_2}$ are arbitrary points with $\tau^2 = (x_1 - x_2)^2 + (y_1 - y_2)^2$, $\cos\theta = (x_2 - x_1)/\tau$ and $\sin\theta = (y_2 - y_1)/\tau$, then

$$\underset{\sim}{u} = \begin{pmatrix} u \\ v \end{pmatrix} = A \begin{pmatrix} u_{\parallel} \\ u_{\perp} \end{pmatrix} = A \tilde{\underset{\sim}{u}} \quad \text{where} \quad A = \begin{pmatrix} \cos\theta & -\sin\theta \\ \sin\theta & \cos\theta \end{pmatrix}.$$

Then
$$R(\underset{\sim}{x_1}, \underset{\sim}{x_2}) = \frac{1}{9^2} E \underset{\sim}{u}(\underset{\sim}{x_1}) \underset{\sim}{u}^T(\underset{\sim}{x_2}) = \frac{1}{9^2} E A \tilde{\underset{\sim}{u}}(\underset{\sim}{x_1}) \left(A \tilde{\underset{\sim}{u}}(\underset{\sim}{x_2}) \right)^T = A B(\tau) A^T \quad \text{or}$$

$$R(\underset{\sim}{x_1}, \underset{\sim}{x_2}) = \begin{pmatrix} \cos^2\theta \, B_{\parallel}(\tau) + \sin^2\theta \, B_{\perp}(\tau) & \cos\theta \sin\theta \left(B_{\parallel}(\tau) - B_{\perp}(\tau) \right) \\ \cos\theta \sin\theta \left(B_{\parallel}(\tau) - B_{\perp}(\tau) \right) & \sin^2\theta \, B_{\parallel}(\tau) + \cos^2\theta \, B_{\perp}(\tau) \end{pmatrix} \tag{4}$$

which is the general form for the autocorrelation matrix for a homogeneous, isotropic two dimensional velocity field. It involves two functions $B_{\parallel}$ and $B_{\perp}$ which we will estimate below from observations. Further it involves the separation τ and the orientation θ of the two points $\underset{\sim}{x_1}$ and $\underset{\sim}{x_2}$ at which the autocorrelation is being evaluated. It may seem strange that θ enters the statistics for an isotropic field. The condition of isotropy does not imply that $E u(0,0) u(\tau, c)$ equals $E u(c, 0) u(0, \tau)$ however. A rotation of coordinates affects both the velocity and the position vectors. A valid statement is $E u(c, 0) u(\tau, 0) = E v(0, 0) v(c, \tau)$ See figure 15.

There is another constraint on the spatial correlation function. Let $\underset{\sim}{u_i} = (u_i, v_i)$ be the velocities at any set of points $\underset{\sim}{x_i}$, $i = 1, ,N$ and let δ_i, η_i be arbitrary real numbers. Then the linear sum

$$s = \sum_{i=1}^{N} \delta_i u_i + \eta_i v_i$$

has a variance which can be expressed in terms of R. The added constraint is that $\text{var}(s) \geq 0$ for all choices of $\underset{\sim}{x_i}, \delta_i, \text{ and } \eta_i$. This requires that the matrix consisting of the correlations of the velocity component at any set of points $\{x_i\}$ must be positive definite (all positive eigenvalues), and is equivalent to the condition that the two dimensional spatial power spectrum of velocity be positive for all pairs of wave numbers (n_x, n_y).

Contradictions can arise if correlation functions are used which do not satisfy this constraint. For example, suppose we wish to consider a velocity field for which $B_{\parallel}(0) = 1$, $B_{\parallel}(L) = 0.9$ and $B_{\parallel}(2L) = 0.5$. The attempt to evaluate the variance of $s = u(0,0) - 1.5 u(L,0) + 0.9 u(2L, 0)$ in terms of these correlations produces a negative result. Since variance is intrinsically positive, we must conclude that no velocity field could have the presumed correlations.

As an example of an analytical form for R which satisfies the positive definite constraint and bears some resemblance to reality, define

$$B_{\parallel}(\tau) = e^{-(\tau/A)^2} \quad , \quad B_{\perp}(\tau) = \left(1 - 2\left(\frac{\tau}{A}\right)^2\right) e^{-(\tau/A)^2} \quad , \quad A \sim 600 \text{ km} \; .$$

This example was constructed by taking a stream function Φ with the positive definite correlation function $R(\tau) = e^{-\tau^2/A^2}$. The corresponding power spectrum is the Hankel transform of $e^{-\tau^2/A^2}$. This is $\pi A^2 e^{-\omega^2 A^2/4}$, $(\omega^2 = m_x^2 + m_y^2)$, which is always positive. Now define velocity components $u = -\partial\Phi/\partial y$, $v = \partial\Phi/\partial x$ and deduce $B_{\parallel}(\tau) = -\frac{1}{\tau}\frac{\partial R(\tau)}{\partial \tau}$ and $B_{\perp}(\tau) = -\frac{\partial^2 R(\tau)}{\partial \tau^2}$.

<u>5.3.3.1 Estimates of the autocorrelation functions.</u>

In order to estimate the autocorrelation matrix, simultaneous velocity observations are required at pairs of points separated by distances ranging from roughly 1 to 10^3 kilometers. We present data from the 1979 buoy program and from AIDJEX which define the functions $B_{\parallel}$ and $B_{\perp}$ only for distances exceeding 100 kilometers. The 1979 data were first interpolated to give velocity estimates at a uniform grid in space and time.

$$\underline{u}_{ijk} = u(x_i, y_j, t_k) \; . \quad \Delta x = \Delta y = 400 \text{ km} \; , \quad \Delta t = 1 \text{ day} \; , \quad i = 1, \cdots N_x \; , \; j = 1, \cdots N_y \; , \; k = 1, \cdots N_t \; .$$

The mean velocity over all points i, j, k was removed. Then for lags ℓ, m, n the lagged correlations were found using

$$R_{\ell, m, n} = \frac{1}{N_x N_y N_t} \sum_{i=1}^{N_x-\ell} \sum_{j=1}^{N_y-m} \sum_{k=1}^{N_t-n} \underline{u}_{i+\ell, j+m, k+n} \; \underline{u}_{ijk}^T$$

For these calculations $N_x = 7$, $N_y = 4$, and $N_t = 200$. The results are sketched in figure 16 for the lags $\ell = 1, \ldots, 7$, $m = n = 0$, and $\ell = n = 0$, $m = 1, \ldots, 4$. The results show that $E\,u(0,0)u(\tau,0)$ and $E\,v(0,0)v(0,\tau)$ are similar functions of τ, and that $E\,v(0,0)u(\tau,0)$, $E\,u(0,0)v(0,\tau)$, $E\,u(0,0)v(\tau,0)$, and $E\,v(0,0)u(0,\tau)$ are all small. These observations are roughly consistent with the assumption that the field is homogeneous and isotropic. We will proceed then on the assumption, supported by these data, that the ice has a homogeneous, isotropic velocity field with the functions $B_{\parallel}$ and $B_{\perp}$ empirically determined from figure 16 .

Correlations for the AIDJEX data were constructed by choosing two of the ice camps, resolving their velocities into components parallel and perpendicular to the line joining the camps, and correlating these components.

These correlations are also plotted in figure 16.

5.3.3.2 Applications of the space correlation.

The spatial autocorrelation function is the basis for sound experiment design and data processing. For instance, suppose observations of velocity u_i are made at N points $\underset{\sim}{x}_i$ with independent zero mean errors having variance σ^2. Estimates of velocity are to be made at arbitrary points $\underset{\sim}{x}$ using these observations. What is the maximum estimation error? We use the tools developed earlier. To estimate the u component of velocity at $\underset{\sim}{x}$, we use the observations $u_1, \cdots, u_N$ and construct the matrices

$$
\begin{pmatrix}
R_{u_1 u_1} + \sigma^2 & R_{u_1 v_1} & R_{u_1 u_2} & \cdots\cdots & R_{u_1 v_N} \\
R_{v_1 u_1} & R_{v_1 v_1} + \sigma_2 & R_{v_1 u_2} & & \\
R_{u_2 u_1} & R_{u_2 v_1} & & & \\
\vdots & & & & \\
\vdots & & & & \\
R_{v_N u_1} & \cdot \quad \cdot \quad \cdot \quad \cdot & \cdots & \cdot & R_{v_N v_N} + \sigma^2
\end{pmatrix}
\begin{pmatrix}
\alpha_1 \\ \beta_1 \\ \cdot \\ \cdot \\ \cdot \\ \alpha_N \\ \beta_N
\end{pmatrix}
=
\begin{pmatrix}
R_{u u_1} \\ R_{u v_1} \\ R_{u u_2} \\ \cdot \\ \cdot \\ R_{u u_N} \\ R_{u v_N}
\end{pmatrix}
$$

where $R_{u_i v_j} = E\, u(\underset{\sim}{x}_i) v(\underset{\sim}{x}_j)$ etc. as given by Eq. 4 . The estimation error variance is given by Eq. 2 . Figure 17 shows how the maximum estimation error depends on the separation between measurement stations and on the measurement accuracy. The curve labelled $\sigma/\varrho^2 = 0$ refers to the idealized condition in which the measurement errors are zero. Thus it represents the interpolation error which is due to the intrinsic spatial variability of the velocity field.

The standard deviation of the ice velocity itself is about $\varrho \sim 10$ cm sec^{-1}. A reasonable observational goal is to keep the interpolation errors below 2 or 3 cm sec^{-1}. This can be achieved if the raw measurements of velocity are good to about 3 cm sec^{-1} and the grid spacing is about 400 km. At larger grid spacings the interpolation accuracy deteriorates rapidly.

5.4 Deformation

The differences in velocity from place to place are responsible for the characteristic morphology of the ice. When the velocity difference between neighboring pieces of ice is such that they tend to move apart, a lead forms and widens exposing the ocean surface to the atmosphere. During the winter, ice growth is rapid over open leads. If the motion changes--perhaps because

of a change in the winds--so that these pieces of ice move toward each other, the open lead will close, and any new ice which formed there will need to rearrange itself to occupy a smaller area. Typical mechanisms for this rearrangement are rafting where one part of the new ice sheet overrides the other, and ridging where the ice is crushed into pieces which pile into ridges rising a meter or two above and sometimes many meters below the surrounding ice. Ridging and rafting are not restricted to thin ice. If the closing motion continues, the original pieces of ice come in contact and one may override the other or, by grinding together, pieces may break off and pile up and down to form a ridge. The essential ideas here are that the ice accommodates divergent motion by increasing the area of open water rather than by stretching and thinning. It accommodates convergent motion by reducing the area of open water and by ridging and rafting. These processes link the morphology of the ice, characterized by such features as floes, ridges, and leads, to the spatial differences in the ice velocity. By studying the spatial variations in velocity we may be able to understand better why the ice pack has the form it does.

There is a second reason for studying the deformation of sea ice. As the ice pack deforms, stresses develop within it which tend to oppose the deformation. These stresses figure into the local balance of forces and therefore affect the motion of the ice. To be more precise, the balance of forces equation contains terms of the form $\partial \sigma_{ij}/\partial x_i$ where σ_{ij} is the stress tensor. The stresses are in turn related to the ice motion by a constitutive law

$$\text{stress} = F(\text{deformation}).$$

One of the motivations for AIDJEX was to investigate the function F from a theoretical point of view and by using observations of the deformation and indirect estimates of the stress (see Rothrock et al., 1980).

The concepts which have been applied to the study of the spatial variations in ice velocity are those appropriate to the analysis of the deformation of a continuum. The fundamental concepts are the partial derivatives of $u(x,y,t)$ and $v(x,y,t)$ with respect to x and y. The line of thought is that a description of the large scale deformation in terms of large scale average derivatives should give some idea of how much opening and closing is going on on smaller scales and some idea of the state of stress. For

example under a purely divergent motion only leads are formed. During a purely convergent motion no leads are formed. On a small scale, shearing along a crack is of no morphological consequence. But large scale shearing is often expressed locally by opening at some cracks and closing at others.

Mathematical formulation of these ideas requires two steps. Required first is an appropriate quantitative description of the large scale deformation in terms of observable parameters. The second requirements is for a functional relationship giving the opening, closing, or state of stress in terms of the observable parameters.

Current practice is to describe the motion in terms of the large scale strain rate invariants, which themselves are constructed from the large scale velocity derivatives. The first invariant

$$E_I = \frac{\partial u}{\partial x} + \frac{\partial v}{\partial y}$$

quantifies the large scale divergence and convergence, and the second invariant

$$E_{II} = \left[\left(\frac{\partial u}{\partial x} - \frac{\partial v}{\partial y} \right)^2 + \left(\frac{\partial u}{\partial y} + \frac{\partial v}{\partial x} \right)^2 \right]^{1/2}$$

quantifies the rate of shearing. A useful alternative pair of invariants is $(|E|, \theta)$, where

$$|E| = \left[E_I^2 + E_{II}^2 \right]^{1/2}$$

expresses the total rate of deformation and

$$\theta = \tan^{-1} \frac{E_{II}}{E_I} \qquad 0 \leq \theta < \pi$$

indicates whether the motion is predominantly divergence $\theta \sim 0$, shear $\theta \sim \pi/2$ or convergence $\theta \sim \pi$.

In the theory presented by Thorndike et al., 1975, opening and closing are assumed to be known functions of θ and proportional to $|E|$.

$$A = \text{total opening} = |E| \, \alpha_o(\theta) \ ,$$

$$C = \text{total closing} = |E| \, \alpha_T(\theta) \ .$$

The functions α_o and α_T which give the total opening and closing in terms of the strain rate invariants may have a form somewhat as sketched in figure 18. There is not much hard evidence to base these sketches on. In

fact the functional relationships for A and C in terms of $|E|$ and θ can only be regarded as approximate since they do not take into account the actual geometry of the floes in the region being considered. Different regions with different geometries will respond differently to similar large scale strain rates.

In practical applications of these ideas the procedure has been to take measured velocities at several points in a region of interest—perhaps the three corners of a 100 km triangle. Velocity derivatives are estimated from the measured velocities. The estimated velocity derivatives are combined to form the strain rate invariants $|E|$ and θ, and these are used to find the rates of opening and closing A and C, and the state of stress $\mathcal{T}$.

In the following sections we reexamine some of these ideas, particularly the notion of velocity derivatives, the influence of the ice pack geometry on opening and closing, and the difficulties in basing inferences about these quantities on small numbers of measurements.

5.4.1 Velocity derivatives

Since the ice pack is made up of discrete pieces moving relative to each other, the variations in velocity have two types:

1) for any x_1 and x_2 on the same rigid piece, the linear relation

$$\underline{u}(\underline{x}_2) - \underline{u}(\underline{x}_1) = \begin{pmatrix} \cos\omega & -\sin\omega \\ \sin\omega & \cos\omega \end{pmatrix} (\underline{x}_2 - \underline{x}_1) \qquad \text{must hold, where } \omega$$

is a constant related to the rate of rotation of the rigid piece.

2) for x_1 and x_2 on separate pieces,

$$\underline{u}(\underline{x}_2) - \underline{u}(\underline{x}_1) \qquad \text{is arbitrary.}$$

$\mathcal{P}$ If we select a random point (x,y) on an ice floe, the partial derivative of velocity,

$$\frac{\partial u}{\partial x}(x,y,t) = \lim_{h \to 0} \frac{u(x+h,y,t) - u(x,y,t)}{h}$$

is well defined because for small enough h, (x,y), and $(x+h,y)$ almost always lie on the same floe and the linearity of the first type of motion mentioned above implies the existence of the limit. Thus the partial derivative exists, but it describes only the rigid body rotation of a floe. It

says nothing about the relative motion between floes which is after all the motion causing the opening and closing and the exchange of momentum between floes.

To include the effect of velocity differences between floes we cannot let h become arbitrarily small. Consider the velocity increment $u(x+h,y,t) - u(x,y,t)$ where (x,y) is fixed and h begins at 100 km and decreases to the smallest value h_0 such that $(x+h_0,y)$ and (x,y) lie on separate floes. This increment captures the variation in velocity from floe to floe and has nothing to say about the rigid rotation of the floe (x,y) lies on. The velocity increment will generally decrease as h approaches h_0, and we can examine the characteristic rate of decrease by evaluating the variance $E\left(u(x+h,y,t) - u(x,y,t)\right)^2$. If this quantity is proportional to h^2 for small h, the velocity at least has a derivative in the mean square sense.

The best data available for examining the variance of velocity increments for a range of spacings were extracted from SEASAT synthetic aperture imaging radar by Hall and Rothrock. By comparing two images separated by three days, they were able to measure the displacement of enough ice features to resolve the full spatial detail in one dimension of the ice motion. After interpolating to evenly spaced points x_i their data have the form

$$\{ u(x_i), v(x_i) \} \qquad i=1,\cdots,N \ , \quad \Delta x = 2 \text{ km}.$$

Given $h = 1, \ldots,$ the h-increments were defined as

$$I_u(h,i) = u(x_{i+h}) - u(x_i)$$
$$I_v(h,i) = v(x_{i+h}) - v(x_i).$$

The variance of the increments was estimated from the $\{ I_u(h,i), I_v(h,i) \}, \ i=1, \cdots N-h$ with the results plotted in figure 17. The linearity of the log-log plot for small h supports a power law relationship with $\text{var}(I(h)) = c\,h^\alpha$ with α in the neighborhood of 1.1 ± 1.5. It appears then that the increments do not decrease as fast as h^2, and therefore the velocity does not have a derivative in the mean square sense.

The statement just made for the variance of increments can be recast in terms of the autocorrelation function. It implies that for small r

$$\beta_{||}(r) \ , \quad \beta_{\perp}(r) \ \sim \ 1 - \tfrac{c}{2} r^\alpha$$

thus helping to define the shape of $\mathcal{B}_\parallel$ and $\mathcal{B}_\perp$ at $\tau = 0$. At $\tau = 0$, $\mathcal{B}_\parallel$ and $\mathcal{B}_\perp$ have the value unity, are continuous, have a continuous first derivative of zero, but fail to have a second derivative.

5.4.2 Velocity differences

The definition of the derivative as a limit could be discarded in favor of a velocity difference over a finite distance,

$$u_{x,L}\ (x,y,t) = \frac{1}{L}\left[u(x+L,y,t) - u(x,y,t) \right]$$

and similar definitions for $u_{y,L}$, $v_{x,L}$, and $v_{y,L}$.

There is no question about the existence of these differences. Definitions for strain rate invariants follow naturally by associating $u_{x,L}$ with $\partial u / \partial x$ etc. in the earlier definitions. When L is chosen to be of order 100 km, these definitions can be used to describe the large scale deformation.

There are several problems with this approach. First, the L-differences carry no information about smaller scales. Second, no basis has been given for choosing a particular value for L. Third, measurements of velocity are rarely available at uniformly spaced points. Still most analyses of sea ice strain have been done with a length scale implicitly fixed by the scale of the observations. To interpret these analyses we must determine the role played by L.

Consider the covariances between the various L-differences. These follow from the covariance structure of the velocity itself. For example

$$E\, u_{x,L}(0,0,t)\, u_{x,L}(\tau,0,t) = \frac{1}{L^2} E\left(u(L,0,t) - u(0,0,t) \right)\left(u(\tau+L,0,t) - u(\tau,0,t) \right)$$

$$= -\frac{1}{L^2}\left[\mathcal{B}_\parallel(\tau+L) - 2\,\mathcal{B}_\parallel(\tau) + \mathcal{B}_\parallel(\tau-L) \right] . \tag{5}$$

To interpret this equation, suppose the L-difference $u_{x,L}$ is measured at two points separated by a distance τ along the x axis. The right hand side of equation 5 approximates the second derivative of $\mathcal{B}_\parallel$ at τ. For small τ, $\mathcal{B}_\parallel$ is concave down so the two L-differences are positively correlated. At some value of τ, $\mathcal{B}_\parallel(\tau)$ has an inflection point. Over such a distance the L-differences become uncorrelated; at longer distances the L-differences are negatively correlated. This example has been worked

for the $u_{x,L}$ component at points separated along the x-axis, but the same procedure can be used to correlate any two first velocity differences at any two points.

It is apparent from this and figure 16 that quantities related to the L-differences are highly correlated in space only over distances of less than about 400 km. Furthermore this statement is not sensitive to the choice of L, since the expression S will change sign at approximately the same r, independent of L. The correlation length scale for velocity by comparison is roughly twice as large (see figure 16).

The ice velocities are well correlated at distances of up to 100 km, as evidenced by the patterns in the long term ice motion (figures 2-4) and in shorter term motions (see Thorndike and Colony, 1980 for instance). It may seem surpising not to find similar patterns in the strain fields. The reason why such patterns are not found is that the strain field has, by equation 5, and figure 16, a correlation length scale of only a few hundred kilometers. Measurement arrays like the 1979 and 1980 buoy arrays with a buoy spacing of roughly 500 kilometers are too coarse to resolve patterns in the strain field.

For the example just worked we can find the variance of the L-difference by setting $r = 0$.

$$E\, u_{x,L}^{2} = \frac{2q^{2}}{L^{2}}\left(1 - B_{\parallel}(L)\right).$$

The symmetric matrix of covariances between pairs of L-differences at the same point is

	$u_{x,L}$	$v_{y,L}$	$u_{y,L}$	$v_{x,L}$
$u_{x,L}$	$\frac{2q^{2}}{L^{2}}\left[1 - B_{\parallel}(L)\right]$	$-\frac{q^{2}}{2L^{2}}\left[B_{\parallel}(\sqrt{2}L) - B_{\perp}(\sqrt{2}L)\right]$	$\frac{q^{2}}{L^{2}}\left[1 + \bar{B}(\sqrt{2}L) - 2\bar{B}(L)\right]$	0
$v_{y,L}$		$\frac{2q^{2}}{L^{2}}\left[1 - B_{\parallel}(L)\right]$	0	$\frac{q^{2}}{L^{2}}\left[1 + \bar{B}(\sqrt{2}L) - 2\bar{B}(L)\right]$
$u_{y,L}$			$\frac{2q^{2}}{L^{2}}\left[1 - B_{\perp}(L)\right]$	$-\frac{q^{2}}{2L^{2}}\left[B_{\parallel}(\sqrt{2}L) - B_{\perp}(\sqrt{2}L)\right]$
$v_{x,L}$				$\frac{2q^{2}}{L^{2}}\left[1 - B_{\perp}(L)\right]$

where $\bar{B} = \frac{1}{2}\left(B_{\parallel} + B_{\perp}\right)$.

This matrix can be evaluated at $L = 400$ km for example by reading points from the plotted functions $B_{\parallel}$ and $B_{\perp}$ in figure 16.

$$
\begin{array}{c|cccc}
 & u_{x,L} & v_{y,L} & u_{y,L} & v_{x,L} \\
\hline
u_{x,L} & 3.9\times10^{-14}\,\text{sec}^{-2} & -0.8\times10^{14}\,\text{sec}^{-2} & 1.4\times10^{14}\,\text{sec}^{-2} & 0 \\
v_{y,L} & & 3.9\times10^{14}\,\text{sec}^{-2} & 0 & 1.4\times10^{14}\,\text{sec}^{-2} \\
u_{y,L} & & & 6.1\times10^{-14}\,\text{sec}^{-2} & -0.8\times10^{14}\,\text{sec}^{-2} \\
v_{x,L} & & & & 6.1\times10^{14}\,\text{sec}^{-2}
\end{array}
$$

$$L = 400\ \text{km}$$
$$q^2 = 10^2\ \text{cm}^2\,\text{sec}^{-2}$$

The covariance matrix for the L-differences illustrates several properties of the way the ice deforms. Notice that the variances of the parallel differences $u_{x,L}$ and $v_{y,L}$ are smaller than the perpendicular differences $u_{y,L}$ and $v_{x,L}$. The parallel differences relate to the linear stretching and contracting of the ice pack. The perpendicular differences relate to shear and rotation. Apparently the second type of motion is greater, but recall the word of caution given earlier that the interpretation of this kinematic evidence is ambiguous. We cannot say whether the observed motion reflects some property of the ice pack or some characteristic of the driving forces.

With the L-differences one could define L-strains in a natural way. The statistics in Table IV of the L-strains follow from the above matrix. These values predict, on the basis of the spatial correlations above, that the large scale divergence will typically be smaller than the vorticity and shear, a prediction verified by many different sets of observations.

Table IV

L-strain		variance	L-strain in percent per day for various L (km), using $q^2 = 10^2\ \text{cm}^2\,\text{sec}^{-2}$			
			100	200	400	800
divergence	$u_{x,L} + v_{y,L}$	$\frac{q^2}{L^2}\left[4 - 4B_{\parallel}(L) - B_{\parallel}(\sqrt{2}L) + B_{\perp}(\sqrt{2}L)\right]$	1.6	2.2	2.2	1.6
vorticity	$u_{y,L} - v_{x,L}$	$\frac{q^2}{L^2}\left[4 - 4B_{\perp}(L) + B_{\parallel}(\sqrt{2}L) - B_{\perp}(\sqrt{2}L)\right]$	4.3	3.7	3.2	2.2
shear	$u_{x,L} - v_{y,L}$	$\frac{q^2}{L^2}\left[4 - 4B_{\parallel}(L) + B_{\parallel}(\sqrt{2}L) - B_{\perp}(\sqrt{2}L)\right]$	3.1	3.0	2.6	18
	$u_{y,L} + v_{x,L}$	$\frac{q^2}{L^2}\left[4 - 4B_{\perp}(L) - B_{\parallel}(\sqrt{2}L) + B_{\perp}(\sqrt{2}L)\right]$	3.4	3.1	2.8	20

5.4.3 Deformation measurements

Several studies have been made over the past decade or so using observation of velocity at an array of stations, with the objective of monitoring the large scale deformation of the region covered by the array. While it is never stated just this way, the implicit definition of large scale deformation appears to involve spatially averaged derivatives over the region,

$$\overline{\frac{\partial u}{\partial x}} = \frac{1}{A} \int_R \frac{\partial u}{\partial x} \, da$$

where A is the area of the region R sampled by the array. Similar expressions define the other large scale average velocity gradients. Application of the Green-Gaus theorem implies

$$\overline{\frac{\partial u}{\partial x}} = \frac{1}{A} \oint_C u \, \underset{\sim}{n} \cdot \underset{\sim}{\hat{\imath}} \, dl \tag{6}$$

where $\underset{\sim}{n}$ is the outward normal to the perimeter C of R , and $\underset{\sim}{\hat{\imath}}$ a unit vector in the x direction.

Note the difference between the L -difference and the large scale average derivative. The former can be measured exactly as $u(x+L,y) - u(x,y)$; the latter requires measurements at every point around a closed curve. In the next section we will discuss how many measurements are required to achieve a desired accuracy in the large scale deformations. But first we review some of the results of the studies just alluded to.

In these studies the deformation estimates were made by finding the linearly varying velocity field which most closely fit the observed velocities at an array of points within R.

$$\underset{\sim}{u}(x) = \underset{\sim}{u_\bullet} + M \underset{\sim}{x}$$

where the matrix M contains the four large scale average velocity partial derivatives. M and $\underset{\sim}{u_\bullet}$ are determined using a least squares fit of the observed velocities $\underset{\sim}{u}$ and positions $\underset{\sim}{x}$. The strain rate invariants were then computed from the elements in M .

The values, given in Table $\mathcal{I}$, confirm some of the results deduced above from the observed spatial correlation functions. For example it is clear that the vorticity is generally several times as large as the divergence. The standard deviation of the divergence and the shear are roughly the same size, but the mean shear is much larger than the mean divergence in most cases.

Table V. Statistics of sea ice deformation

Length scale diameter (km)	Season	Divergence		Shear		Vorticity		Strain magnitude mean	Experiment
		mean	st.dev.	mean	st.dev.	mean	st.dev.		
20	spring	--	0.65	--	0.86	--	1.1	--	AIDJEX 1972
100	spring	--	0.43	--	0.54	--	0.61	--	AIDJEX 1972
200	winter	0.07	1.0	1.6	1.6	-0.52	2.0	2.1	1975 AIDJEX manned array
	summer	-0.03	1.6	3.5	2.2	--	--	--	
800	winter	0.02	0.56	1.0	0.86	--	--	1.3	1975 AIDJEX buoy array
	summer	0.16	1.0	1.6	0.86	--	--	2.2	
800	winter	0.07	0.58	0.77	0.54	--	--	1.1	1962-64 F3, NP-10, Arlis II
	summer	0.06	0.80	1.0	0.68	--	--	1.5	
1000	winter	0.02	0.45	0.95	0.82	-0.78	1.5	1.1	1979 buoys
	summer	-0.11	0.76	1.5	0.95	--	--	1.9	

Sources: Hibler, et al., 1974; Colony and Thorndike, 1981; Maykut, 1981.

The distribution of the invariant θ is plotted in figure 20 . Note that nearly always $\pi/4 < \theta < {}^3\pi/4$. In this range, the two principal values of the strain rate tensor have opposite signs. The figure indicates that it is almost always the case that when the ice pack is extending in one direction, it is contracting in the perpendicular direction. Hibler et al., 1974 also comments on this for strain measurements on a 20 kilometer scale.

It is also evident from Table V that the summer values are usually somewhat greater than the winter-spring values. Presumably the ice pack is weaker and offers less resistance to deformation in the summer. (The alternative hypotehsis, that the driving forces are larger in the summer, is not true.)

The mean quantities in Table V produce large strains over the course of a year. The year long deformations at the AIDJEX arrays are shown in figure 21 . The region experienced a net clockwise rotation of about 35°. The principal deformation involved a stretching of about 90% in the east-west direction and a contraction of about 40% in the north-south direction. The net divergence was not significantly different from zero. The two nested arrays expressed similar deformations. .

Deformation estimates at a number of points in the central basin for the years 1979 and 1980 are presented in figure 22. The strain ellipses typically show large shear and small divergence. The only pattern evident in the figure is the similar alignment of the major principal axis of shear for the five points closest to the pole.   We should not expect to see any patterns in the deformation displayed on this scale. Recall that the spatial correlation function for L-differences has a length scale of only about 400 kilometers. The deformations at points separated by greater distances should evolve more or less independently.

5.4.4 Interpretation of deformation measurements

A number of authors have confronted the difficulties of describing the deformation of this decidedly discontinuum. Nye (1973) for instance, puts forward a definition of "strain on a length scale L ." By first smoothing the velocity field using a kernel of length scale L , he obtains a new velocity field which is differentiable and for which the usual notions of deformation based on partial derivatives are valid. Papers by Hibler et al., 1974 and Thorndike and Colony, 1977 take a similar point of view by attempting to partition the ice deformation into two parts. The first part is assumed to be associated with the spatial variation of the atmospheric and oceanic

forcing fields and with the geometry of the basin, to have a characteristic length of 10^3 km, and to be differentiable. The second part is associated with the irregular, discrete geometry of the ice pack. It has length scales less than 10 km and is characterized by discontinuous variations in velocity. In these papers, the first kind of variation is referred to as the large scale, underlying, continuum, or linear part of the velocity field, while the second is referred to as the small scale, local, perturbation, fluctuating, or non linear part. Velocity variations of the first type are regarded as signal and those of the second type as noise. This nomenclature reflects the hope that any physical process of interest can be parameterized in terms of the large scale signal, with small scale noise only making it difficult to measure the signal well.

This convention obscures the true nature of the velocity field which is that it has variations on all length scales, with a smooth decrease in amplitude for decreasing length scales. There is no clear division between large and small scale. Furthermore there is no clear reason to associate large scale with signal and small scale with noise. For studies involving the actual opening and closing of leads, the small scale phenomena may indeed be the signal and it cannot readily be parameterized by the large scale motion.

Perhaps a better conceptual model of the spatial structure of the ice velocity is a system which accepts a smooth input and produces a discontinuous output. $\Big($A simple example of such a system is the greatest integer function:

$$[x] = \text{greatest integer less than or equal to } x \; . \Big)$$

—— The shift in emphasis from the earlier model is this. The earlier model viewed the velocity as the sum of separate contributions, one smooth, one discontinuous. The alternative views the velocity as a discontinuous response to a smooth input. This point of view may lead more naturally to phenomenological descriptions of the properties of the ice pack, through a comparison of the input and output fields. To my knowledge this has not been attempted because data with adequate spatial resolution of the velocity field are still too scarce. Such a study would not explain why the velocity field had certain properties. That explanation must be based on rather deeper understanding of the geometry of the ice pack and the forces which act between floes than we have at present. Still it would be useful to compare some of the properties of the ice velocity with properties of the external driving forces, i.e., the geostrophic wind and the ocean currents.

5.4.5 . Errors in estimating the large scale deformation

The large scale deformation estimates of the previous section are subject to sampling variations since they depend on the particular array of measurements points. There have been several attempts to quantify the sampling errors. Hibler et al., 1974; Nye, 1975; and Thorndike and Colony, 1977 examined the departures of the measured velocities from the best fit linear relationships. These departures, called residuals, homogeneity variations, or nonlinear fluctuations, represent the variability of the actual velocity field on scales smaller than the diameter of the region of interest.

From observations over a 200 km scale taken during the spring of 1972, Hibler et al. found root-mean-square velocity residuals of 0.06 cm sec^{-1}, compared to typical linear changes in velocity $\left(\overline{L \, \partial u / \partial x} \right)$ over 20 km of 0.14 cm sec^{-1}. Thorndike and Colony used observations from a 100 km scale taken during the spring of 1975 and found rms residuals of 0.4 cm sec^{-1} and typical linear changes over 100 km of 1.1 cm sec^{-1}. Their summer values were somewhat larger: 1.1 cm sec^{-1} and 1.8 cm sec^{-1} for the nonlinear and linear contributions. These residuals can be regarded as errors with respect to the large scale average derivatives for the region. When the number of observations is small, the estimated large scale deformations are strongly contaminated by these errors.

Using what we know about the correlation functions for velocity, we can profitably address the sampling question from a different angle. Taking the line integral definition for the large scale velocity derivatives, we ask: how many points around the perimeter of the region must be sampled to resolve the integral to some desired accuracy? Intuition suggests that the measurements should be spaced closely enough to permit good interpolation but not so closely as to be highly redundant. A correlation between velocities at neighboring measurement points of 0.5 might be a fair guess; this would indicate a spacing of about 400 km.

To get a better answer, we estimate the line integral in equation 6 around a circular region of radius r as

$$D_M = \frac{1}{\pi r^2} \sum_{i=1}^{M} u_i \cos \theta_i \frac{2 \pi r}{M} \quad , \quad \theta_i = (i-1)\frac{2\pi}{M} \quad , \; i = 1, \cdots, M.$$

Then as the number of measurements M increases, D_M approaches $\overline{\partial u / \partial x}$. Since D_M is a linear combination of velocity components, we can find its

variance in terms of the variances and covariances of the velocity components at all M points, and these can be evaluated in terms of the correlation functions $B_{\parallel}$ and $B_{\perp}$. Let $\underline{u}$ be the vector involving all $2M$ velocity components, $\underline{A}$ be the vector of coefficients, and R be $E\,\underline{u}\,\underline{u}^T$. Then $D_m = \underline{A}^T\underline{u}$ and $ED_m^2 = \underline{A}^T R \underline{A}$. This calculation has been done for $M = 60$ which was large enough to resolve $\overline{\partial u/\partial x}$. The dependence of $(E\,D_{t,?}^2)^{1/2}$ on the radius r is shown in figure $23a$.

The figure shows that typical values for $\overline{\partial u/\partial x}$ are about 1% per day, decreasing somewhat as the radius of the region increases. Of course this curve is a consequence of the observed functions $B_{\parallel}$ and $B_{\perp}$. The shape of the curve for radii smaller than 100 km remains speculative until more details are known of the behavior of $B_{\parallel}$ and $B_{\perp}$ for small arguments.

The variance of the error in estimating $\overline{\partial u/\partial x}$ using only M points, $E\left(D_M - D_{60}\right)^2$ can be calculated in the same manner simply by redefining the coefficients in the vector $\underline{A}$. These results are presented as a fraction of the signal variance $E\left(D_{60}^2\right)$ in figure $23b$. When M is 3, as was the case for AIDJEX 1972, the 1975-76 manned AIDJEX array, and LOREX 79, and the radius was about 100 km, the ratio of estimation error variance to signal variance was about 0.25. For a radius of 400 km and a spacing between stations of 400 km, $M = 6$, and the ratio of error variance to signal variance is about 0.01. This confirms our intuition that a spacing of 400 km should be adequate to resolve the large scale average velocity gradients quite well.

Figures $23c$ and $23d$ show results obtained in a similar way for the large scale average derivative $\overline{\partial v/\partial x}$ and for the large scale average divergence. Accurate estimation of the large scale average divergence has special importance because of the role it plays in the theory of the ice thickness distribution. If we want to keep the rms error in divergence below say 20% of the rms divergence we require a ratio of variances in figure $23d$ of $0.2^2 = 0.04$. For a region of radius 200 kilometers this level of accuracy can be achieved with 6 measurement stations.

5.4.6 The relationship between measured large scale deformation and total opening and closing

Suppose a region of interest is intersected by a number of cracks, each of which is opening or closing at some rate. If the rates were known, the total rates of opening and closing for the region could be found. In practice we are not able to measure the motion at each crack, but only the motion of a few points in the region. How are we to use these few measurements to estimate the opening and closing?

In an analogous situation in one dimension, we have k cracks each with opening or closing rate u_i, $i=1,\cdots,k$. We can imagine the velocity u to be a random function of x having random discontinuities at random points and being constant between the points. Suppose we have measured only the motion at the end points of the region, an interval of length L . Then

$$A = \text{total opening} = \sum_{i=1}^{k} \max(u_i, 0) \quad ,$$

$$C = \text{total closing} = \sum_{i=1}^{k} \min(u_i, 0) \quad , \tag{7}$$

$$U = \text{net opening or closing} = A + C = \sum_{i=1}^{k} u_i \quad ,$$

and the problem is to estimate A and C given U . At first sight the situation seems hopeless. U clearly contains information about the net opening or closing but not about the total opening and closing. However, knowledge about the random variables $k, u_1, u_2, \cdots, u_k$ can be used to make probabalistic statements about the opening and closing. Suppose for instance k has the Poisson distribution with parameter λ . This means that λL is the average number of cracks in an interval of length L . Then the probability of finding k cracks in a random interval of length L is

$$p(k; \lambda L) = (\lambda L)^k e^{-\lambda L} / k! \quad .$$

If $\lambda L = 0.1$, for instance, the probability of getting $k = 0$ is 0.9051, $p(k=1) = 0.0905$, and $p(k>1) = 0.0045$. Therefore, with high probability, there is either no crack or just one in the interval and the observed value of the velocity difference U would itself indicate the total opening and total closing. Of course for larger λL it becomes more likely that several cracks intersect the test interval, in which case the observed U cannot separate the opening from the closing.

A similar approach for the two dimensional problem is to imagine the ice pack to be crisscrossed by a family of random cracks, defined by the random straight lines

$$x \cos\theta_i + y \sin\theta_i = \tau_i$$

where each θ_i has the uniform distribution on $(0, 2\pi)$ and the normal distances

r_i from the origin to each line form a sequence of Poisson points. Imagine that associated with each crack is a velocity discontinuity μ_i having the Gaussian distribution. This describes a random vector field having structure akin to the velocity field of sea ice. The observations of Hall and Rothrock can be used to estimate the parameters in the Poisson and Gaussian distributions. These random fields have the following properties. They consist of discrete rigid floes. The floes have a distribution of sizes determined by the Poisson field of lines. The Poisson lines are isotropic and homogeneous. The velocity difference between any two points is the vector sum of the velocity discontinuities encountered getting from one point to the other.

At each crack the opening or closing is determined by the projection of the velocity difference vector onto the normal to the crack.

$$\text{opening} = \max\left(0, \quad u_i \cos\theta_i + v_i \sin\theta_i\right)$$

$$\text{closing} = \min\left(0, \quad u_i \cos\theta_i + v_i \sin\theta_i\right)$$

Thus it is a simple matter to evaluate the total opening and closing for any realization of the random field.

Of course one can also imagine measuring the velocity at a few points and constructing the L-strain rate invariants from the observed velocities. In this way one can test for a relationship between the L-strain rate invariants calculated from a few sampled velocities and the total opening and total closing found by tallying up the activity at every crack.

In an attempt to carry out this program, parameter values were taken to be $\lambda = 0.08 \text{ km}^{-1}$, $\mu = 0$, $\sigma^2 = 1$ (arbitrary units)^2. An $L = 100$ km triangle was used to simulate the sampling procedure used during AIDJEX. A large number of random fields were generated.

Each realization of the random field is defined by the sequences of random numbers $k, \theta_i, u_i, v_i, r_i$ for $i = 1, \cdots, k$. Here the θ_i are drawn independently from the uniform distribution on $(0, 2\pi)$. The values for r_i form a Poisson process with parameter λ. This is achieved by drawing the increments $\Delta = r_{i+1} - r_i$ independently from the exponential distribution with density $\lambda e^{-\lambda\Delta}$. The process is terminated as soon as r_k exceeds 100 kilometers since none of the subsequent lines would intersect the 100 kilometer region. Finally the u_i and v_i were drawn independently from the normal distribution with zero mean and unit variance.

For each field the velocity was measured at the three specified points and the L-strain rate invariants $|E|$ and θ were evaluated. Also for each field the total opening and closing were evaluated using eq. 7 . These were normalized by $|E|$ and displayed versus θ in figure 24. For each realization of this random field two points are plotted, $(\theta, A/|E|)$ and $(\theta, C/|E|)$. From the plot it is clear that there are not unique values of $A/|E|$ and $C/|E|$ corresponding to a given θ . Instead there is a distribution of values for $A/|E|$ (and for $C/|E|$), and this distribution changes with θ . The distributions sketched in figure 25, are broad in the sense that probable departures from the mean are at least as large as the mean.

The interpretation of this exercise is that the total opening and closing are only weakly determined by the L-strain rate invariants based on three measurements 100 kilometers apart. Had the relationship been a strong one the distributions in figure 25 would have been narrower, or to say it differently, the points in figure 24 would have clustered more closely around curves like those in figure 18 . It may still be useful to imagine these smooth curves but only with the recognition that the actual opening and closing scatter widely about the imagined curve:

$$\frac{A}{|E|} = \alpha_o(\theta) \qquad + \text{ random error}$$

$$\frac{C}{|E|} = \alpha_r(\theta) \qquad + \text{ random error}$$

where the random terms and the θ-dependent terms make roughly equal contributions to the total opening and closing.

The total opening and closing are an essential part of the theory of the ice thickness distribution. The above results suggest that it will be difficult to estimate the opening and closing accurately. Perhaps the best that can be hoped is to drive the thickness distribution calculations with opening and closing time series which have the right statistical properties even if they may have large errors on a day to day basis. The statistical properties can be inferred from figure 24 . Of course this figure is the consequence of a particular conceptual model motivated by a limited data set—the SEASAT SAR data from early October 1978. More data need to be collected and studied before these ideas can be extended to other times and places with confidence.

5.4.7   The relationship between kinematics and stress

Kinematic data can be used for studying the relationship between stress and strain for sea ice. Suppose for instance that the state of stress tensor σ suitably averaged over some region, is related to kinematic quantities ε and the ice geometry s by some expression of the form

$$\sigma = F(\varepsilon, s) \ .$$

Although σ cannot be measured directly, its divergence $\nabla \cdot \sigma$ can be inferred indirectly from the observed momentum balance when all the other terms in that balance are known. If a particular function F is hypothesized, it can be tested by evaluating both sides of the equation $\nabla \cdot \sigma = \nabla \cdot F(\varepsilon, s)$, the left hand side as a residual from the momentum balance and the right hand side in terms of observed kinematic and ice geometry quantities. This was one of the objectives of AIDJEX (Maykut et al., 1972). In practice the test is difficult to make since neither $\nabla \cdot \sigma$ nor $\nabla \cdot F$ can be deter- mened very accurately from observations. See Rothrock et al., 1980.

Under special circumstances, meaningful tests may be possible, however. When the ice deformation is strongly divergent, ice floes tend to move apart. With no floe-to-floe contacts there can be no $\nabla \cdot \sigma$ forces. The left hand side should differ from zero only by measurement error. These errors are probably small enough to permit a useful test.

Another special situation of interest is when the ice is being forced up against the coasts by the wind. As the ice moves toward the coast it converges, becomes stronger, and eventually becomes strong enough to resist further deformation. If the on shore winds persist, a zone of motionless ice can widen to several hundred kilometers (Pritchard, 1977). In this situa- tion, intuition suggests that the $\nabla \cdot \sigma$ vector should point off shore and should increase in time until it balances the on shore wind stress. With simultaneous ice trajectories at 100, 200, 300 and 400 km from the coast it should be possible to observe the amount of convergence required to pro- duce the required resistance to the wind.

At greater distances from the coasts, there is evidence that the ice stresses embodied in $\nabla \cdot \sigma$ are usually small. Little success is anticipated in trying to observe them. Any stress-strain law which provides adequate resistance to deformation near the shore is probably adequate for full basin

dynamic modelling. The observations may never be adequate to discriminate very selectively between candidate stress-strain laws.

5.5 Discussion

I have tried in this paper to bring together some of what is known about the motion of sea ice. The emphasis has been on the departures of the true motion from the long term mean circulation. This is a comparitively new topic, the investigation of which has only recently been made possible, mainly by the developments of satellite positioning techniques. Perhpas because of its newness, the field lacks a clear agenda of questions to be answered. Instead we are still trying to characterize the motion, to determine the magnitude of the motion on different scales and to identify motions which have some intrinsic interest or are related to other phenomena of interest. It is not surprising that contributors to the field have differred in their approaches to observing and interpreting the motion.

The time and space corelations have been used extensively here for several reasons. First they give a compact description of the motion. In principle, the correlation function involves one time and two space variables, but in practice a great deal of information can be extracted from three functions, each of a single variable: $R(\tau)$, $B_{\parallel}(\tau)$ and $B_{\perp}(\tau)$. Second, these three functions are accessible to observation. Third, prope ies of nearly all kinematic quantities can be deduced from these functions, as illustrated, ad nauseum, in the text. Fourth, these functions form the rigorous basis for answering questions related to interpolation, prediction, and experiment design.

Many of the results presented here are based on sample autocorrelation functions deduced from limited data. The data available for estimating correlations at small space lags (less than 100 km) are meagre indeed. More work along the lines of Hall and Rothrock would help to resolve this part of the correlation function. The behavior of the correlation functions $B_{\parallel}(\tau)$ and $B_{\perp}(\tau)$ in the limit of small τ is an important property of the motion related to the granular nature of the ice pack.

As mentioned in the text, care must be exercised in choosing correlation functions or contradictions (negative variances) can occur. In fact this has happened in some of the calculations done using the correlations tabulated in Table VI with linear interpolation to intermediate distances. This means that the piecewise linear function defined in the table is not positive

Table VI. Spatial correlation functions for sea ice velocity.

Distance (km)	$\beta_\parallel$	$\beta_\perp$
0	1.00	1.00
100	.98	.95
200	.91	.84
400	.68	.51
800	.37	.06
1200	.19	-.09
1600	.10	-.10
2000	.01	-.06
2400	.00	.00

References

AIDJEX Staff, 1972. Station positions, azimuths, weather, 1972 AIDJEX Pilot Study, Preliminary data, _AIDJEX Bulletin No. 14_, 63-208.

Colony, R. and A. S. Thorndike, 1980. The horizontal coherency of the motion of summer arctic sea ice. _J. of Phys. Oceanography_, 10(8), 1281-1289.

Colony, R. and A. S. Thorndike, 1981. Sea ice strains during 1979. _Proceedings of the 6th International Conference on Port and Ocean Engineering Under Arctic Conditions_, Quebec City, Quebec, 27-31 July 1981, 619-628.

Craig, L. W., 1972. High frequency accelerations of arctic pack ice. Master's thesis, Department of Civil Engineering, University of Washington, Seattle.

Doronin, Yu. P. and D. E. Kheisin, 1975. Morskoi Led. (English translation, Sea ice, 1977. Amerind Publishing Co. Pvt. Ltd., New Delhi.) 323 pp.

Hall, R. T., 1980. AIDJEX modeling group studies involving remote sensing data. _Sea Ice Processes and Models_, R. S. Pritchard, Editor; University of Washington Press, Seattle.

Hall, R. T. and D. A. Rothrock, 1981. Sea ice displacement from SEASAT synthetic aperture radar. To appear in _J. of Geophys. Res._

Hastings, A. D. Jr., 1971. Surface climate of the Arctic Basin. Report ETL-TR-71-5, Earth Sciences Division, Geographic Sciences Laboratory, U.S. Army Engineer Topographic Labs, Fort Belvoir, VA.

Hibler, W. D. III, W. F. Weeks, A. Kovacs, and S. F. Ackley, 1974. Differential sea-ice drift. I. Spatial and temporal variations in sea ice deformation. _J. of Glaciology_, 13(69), 437-455.

Hunkins, K., 1967. Inertial oscillations of Fletcher's Ice Island (T-3). _J. of Geophys. Res._, 72(4), 1165-73.

Hunkins, K. and J. Hall, 1971. The navigation of Fletcher's Ice Island (T-3). _AIDJEX Bulletin No. 7_, 47-58.

Hunkins, K. T. Manley, and W. Tiemann, 1979. Observations of position, ocean depth, ice rotation, magnetic declination and gravity taken at the Fram I drifting ice station. _CU-1-79 Technical Report No. 1_, Office of Naval Research, Department of the Navy, 60 pp.

Kolmogoroff, A., 1941. The local structure of turbulence in incompressible viscous fluid for very large Reynolds numbers. _Comptes Rendus (Doklady) de l'Academie des Sciences de l'URSS_, 30(4), 301-305.

Kowalik, Z. and N. Untersteiner, 1978. A numerical study of the M_2 tide in the Arctic Ocean. _Deutsche Hydrographische Zeitschrift_, Vol. 31, 216-229.

Manley, T., 1981. Eddies of the western Arctic Ocean: their characteristics and importance to the energy, heat and salt balance. Doctoral dissertation, Columbia University, 212 pp.

definite. A useful objective would be to find a positive definite analytical form which approximates the observed correlations including the behavior as τ approaches zero.

The Poisson-Gaus model, presented as a way to study the relationships between the local opening and closing and the large scale deformation has suggested that the relationship may be weak. Observations against which to test this suggestion are sorely needed.

References, continued

Martin, P., C. R. Gillespie, A. S. Thorndike, D. Wells, 1978. Position measurements of AIDJEX manned camps using the Navy Navigation Satellite System. AIDJEX Bulletin No. 40, 83-102.

Maykut, G. A., 1981. Large scale heat exchange and ice production in the central arctic, submitted to J. of Geophys. Res.

Maykut, G. A., A. S. Thorndike, and N. Untersteiner, 1972. AIDJEX scientific plan. AIDJEX Bulletin No. 15, 67 pp.

McPhee, M. G., 1978. A simulation of inertial oscillations in drifting pack ice. Dynamics of Atmospheres and Oceans, 2, 107-122.

Nye, J. F., 1973. The meaning of two-dimensional strain-rate in a floating ice cover. AIDJEX Bulletin No. 21, 9-17.

Nye, J. F., 1975. The use of ERTS photographs to measure the movement and deformation of sea ice. J. of Glaciology, 73(15), 429-436.

Nye, J. F., 1976. A coordinate system for two dimensional stress and strain rate and its application to the deformation of sea ice. AIDJEX Bulletin No. 33, 131-143.

Popelar, J., J. Kouba, and D. Wells, 1981. LOREX Satellite Positioning, Draft report, Earth Physics Branch, Department of Energy, Mines and Resources, Ottawa, Ontario, Canada.

Pritchard, R. S., 1977. An estimate of the strength of arctic pack ice. AIDJEX Bulletin No. 34, 94-113.

Rothrock, D. A., 1979. Modeling sea ice features and processes. J. of Glaciology, 24(90), 359-375.

Rothrock, D. A., R. Colony, and A. S. Thorndike, 1980. Testing pack ice constitutive laws with stress divergence measurements. Sea Ice Processes and Models, R. S. Pritchard, Editor; University of Washington Press, 102-112.

Sverdrup, H. U., 1926. Dynamics of tides on the north Siberian shelf, results from the Maud expedition. Geofysiske Publikasjoner IV(5), 75 pp.

Tabata, T., T. Kawamura, and M. Aota, 1980. Divergence and rotation of an ice field off Okhotsk Sea Coast of Hokkaido. Sea Ice Processes and Models, R. S. Pritchard, Editor; University of Washington Press, 273-282.

Thorndike, A. S., 1973. An integrated system for measuring sea ice motions. In Ocean 73, IEEE International Conference on Engineering in the Ocean Environment, IEEE Publ. No. 73 CHO 774-0, 490-499.

Thorndike, A. S. and J. Y. Cheung, 1977. AIDJEX measurements of sea ice motion 11 April 1975 to May 1976. AIDJEX Bulletin No. 35, 1-149.

References, continued

Thorndike, A. S. and J. C. Cheung, 1977. Measurements of sea ice motion 14 May 1976 to 30 November 1976, October 1975 to December 1976, and January 1977 to September 1977. Unpublished data reports, available from the authors.

Thorndike, A. S. and R. Colony, 1977. Estimating the deformation of sea ice. In Proceedings of the Fourth Annual Conference on Port and Ocean Engineering under Arctic Conditions (ed. D. B. Muggeridge, Vol. 1, 506-517. Memorial University of Newfoundland, St. John's.

Thorndike, A. S. and R. Colony, 1980. Arctic Ocean buoy program, data report, 19 January 1979-31 December 1979. University of Washington, 131 pp.

Thorndike, A. S. and R. Colony, 1981. Sea ice motion in response to geostrophic winds. Submitted to J. of Geophys. Res.

Thorndike, A. S. and R. Colony, 1981. Arctic Ocean buoy program, data report, 1 January 1980-31 December 1980. University of Washington, in preparation.

Thorndike, A. S., D. A. Rothrock, G. A. Maykut and R. Colony, 1975. The thickness distribution of sea ice. J. of Geophys. Res, 80(33). 4501-4513.

Tucker, W. B., W. F. Weeks, A. Kovacs, A. J. Gow, 1980. Nearshore ice motion at Prudhoe Bay, Alaska. Sea Ice Processes and Models, R. S. Pritchard, Editor; University of Washington Press, 261-272.

Zubov, N. N., 1943. L'dy arktiki (Arctic ice), Glavsev-morput (Northern Sea Route Administration), Moscow. Translation 1963. U.S. Navy Hydrographic Office Translation 217, available as AD-426-972, from NTIS, Springfield, VA.

winds and ocean currents → | properties of the ice pack | → ice motion →
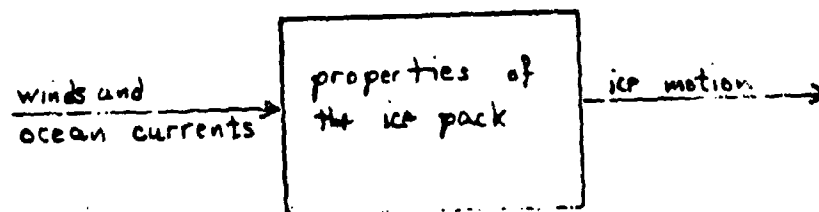
Figure 1.

Figure 2. The general circulation of ice in the Arctic Ocean (from Doronin and Kheisin).
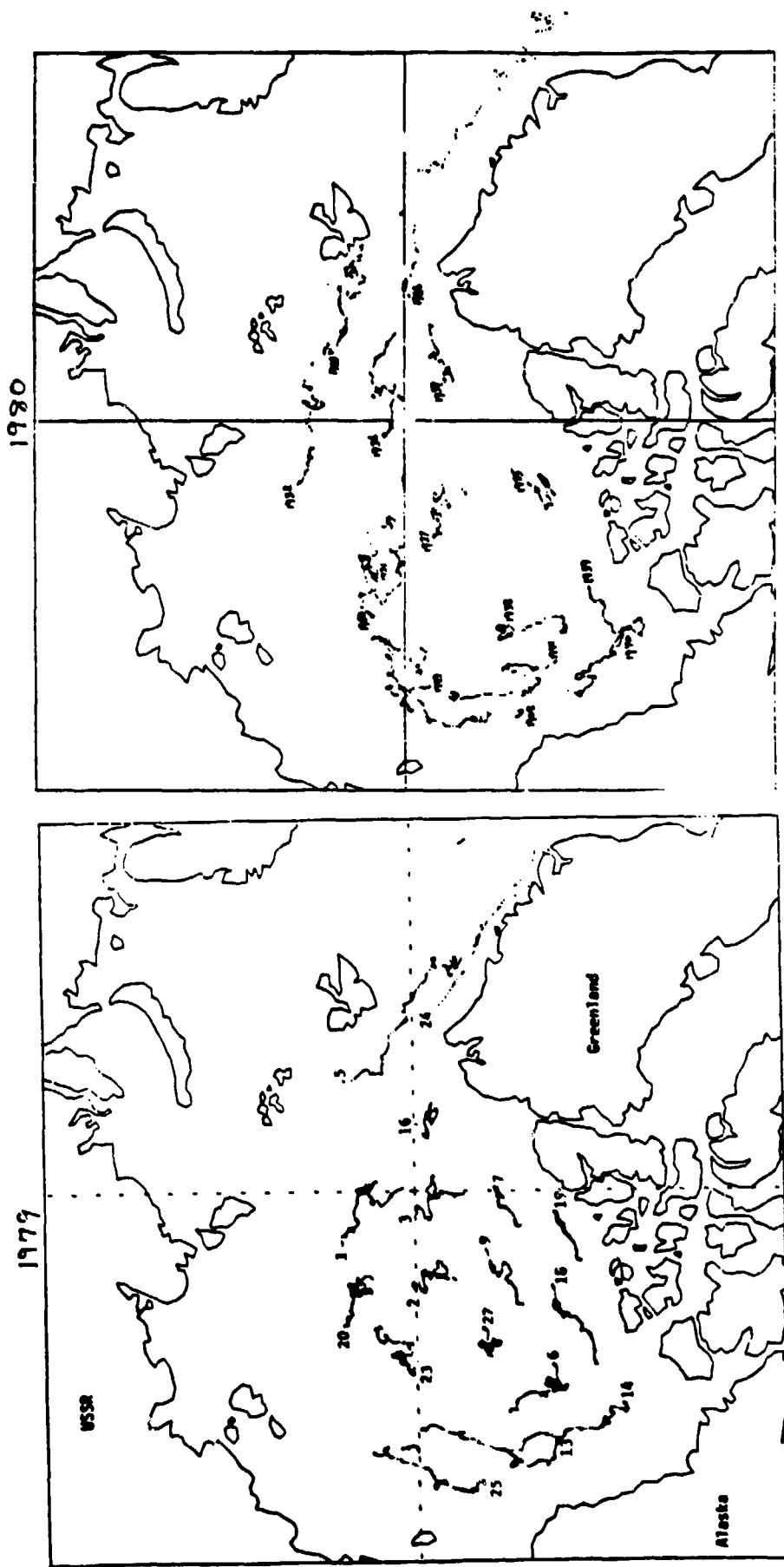
Figure 3. Trajectories for drifting buoys during 1979. Not all buoys operated for the same time period. See Thorndike and Colony, 1980 for details.

Figure 4. Trajectories for drifting buoys during 1980.
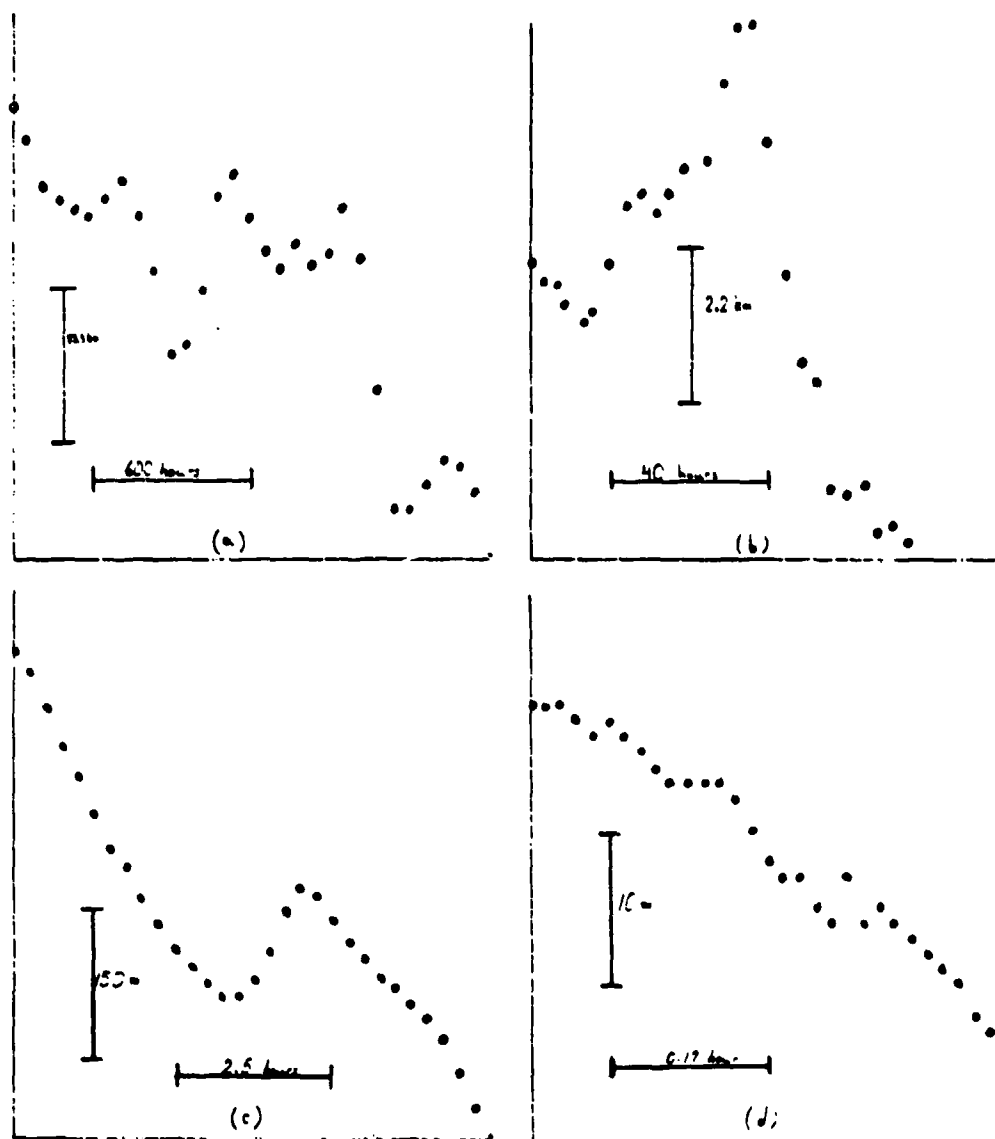
Figure 5. (a) Latitude of ice station Caribou, versus time, 2 Sept-16 Nov 1975. NavSat data, sampling interval, 2.5 days.
(b) Latitude of ice station Big Bear, versus time, 2-15 Sept 1975. NavSat data, sampling interval, 4 hours.
(c) Arbitrary y-coordinate of Big Bear, versus time, 2-3 Sept 1975. Acoustic tracking data, sampling interval 15 minutes.
(d) Arbitrary x-coordinate of Big Bear, versus time, 2 Sept 1975. Acoustic tracking data, sampling interval one minute.
    Only in (d) is the measurement error visible (±3 m).
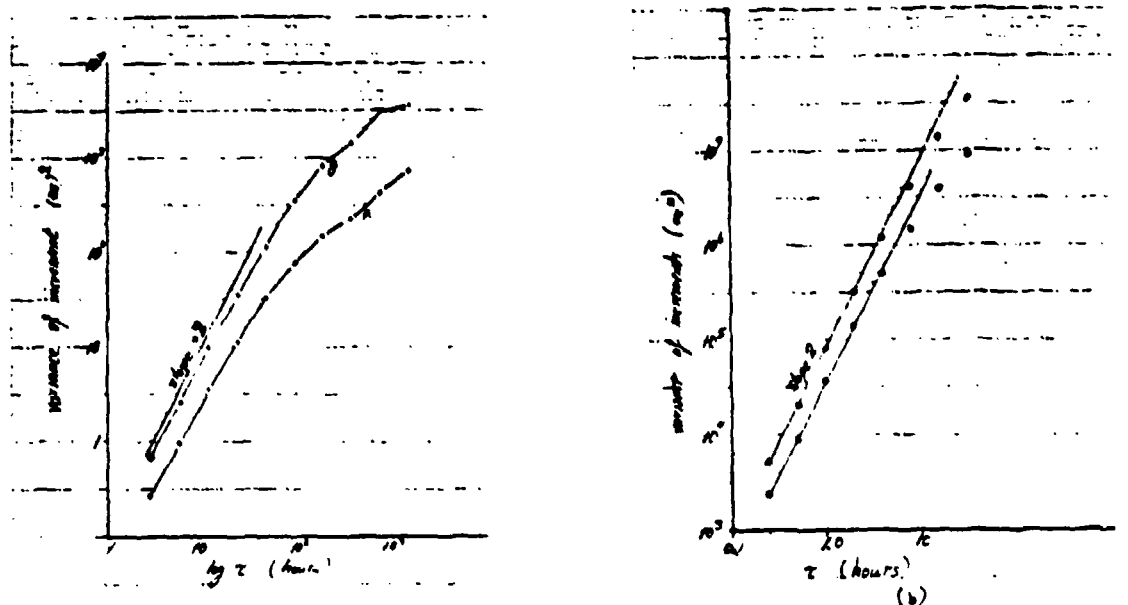
Figure 6. (a) The variance of the increments $x(t+\tau) - x(t)$ and $y(t+\tau) - y(t)$ for ice station Caribou 1975-76. x and y are arbitrary Cartesian coordinates.
(b) As in (a) using precise acoustic tracking at ice station Big Bear, an 8-day period, late summer 1976.
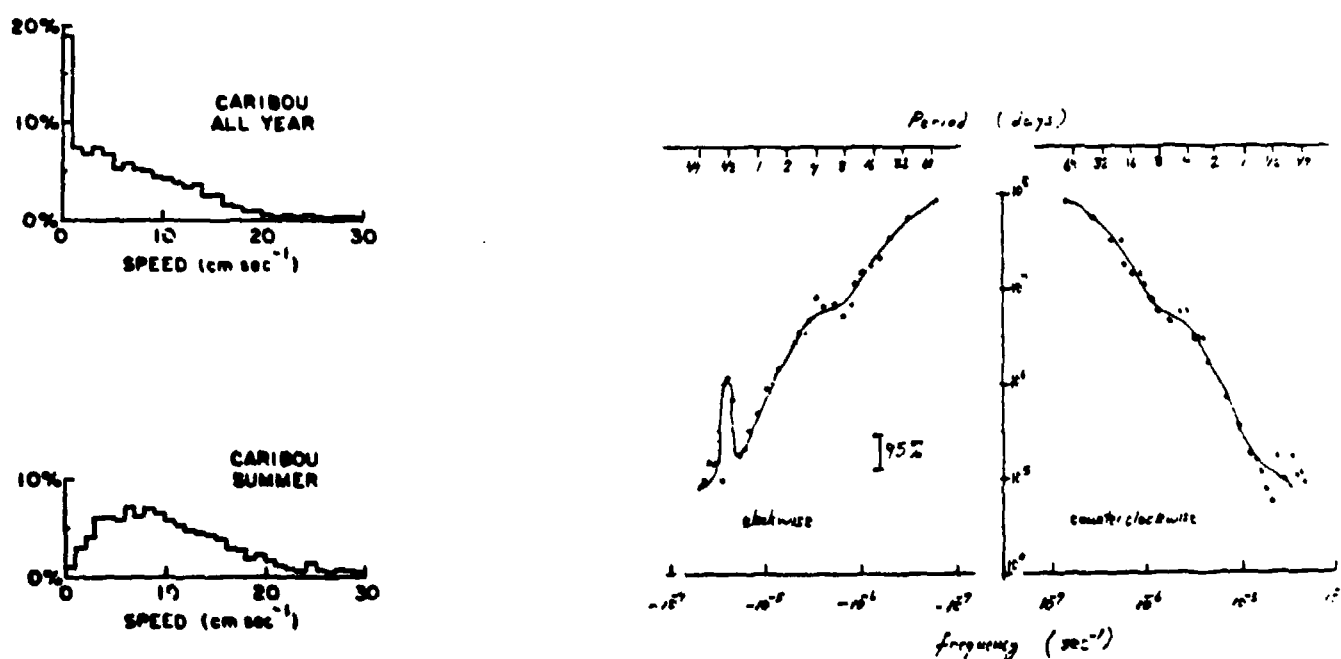
Figure 7. VELOCITY HISTOGRAMS

Figure 8. The power spectral density of the velocity of ice station Caribou 1975-76. The units of spectral density are velocity^2/frequency, cm^2 sec^{-1}. The total velocity variance for these data is 145 cm^2 sec^{-2}.

Fig. 10

Fig. 9
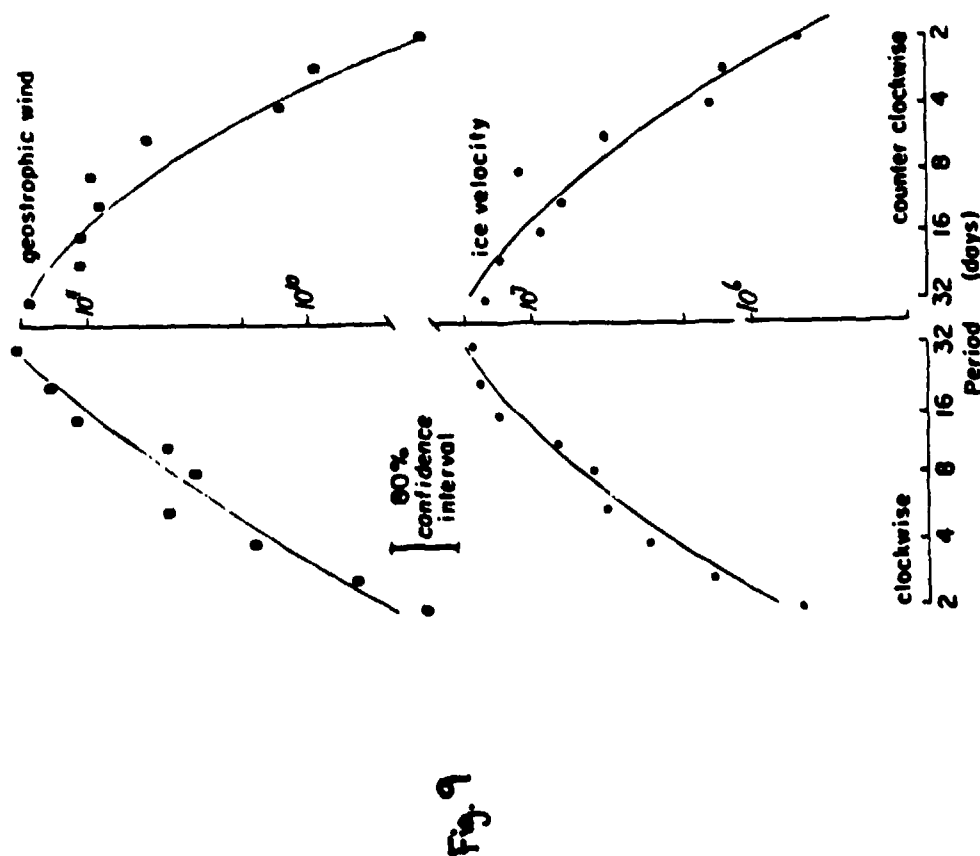
Figure 9. The power spectral densities of the geostrophic wind and the ice velocity, from drifting buoy 1901 during 1979. The units of spectral density are cm²sec⁻¹. The variance of the wind is 53 m²sec⁻². The variance of the ice is 59 cm²sec⁻². From Thorndike and Colony, 1981.
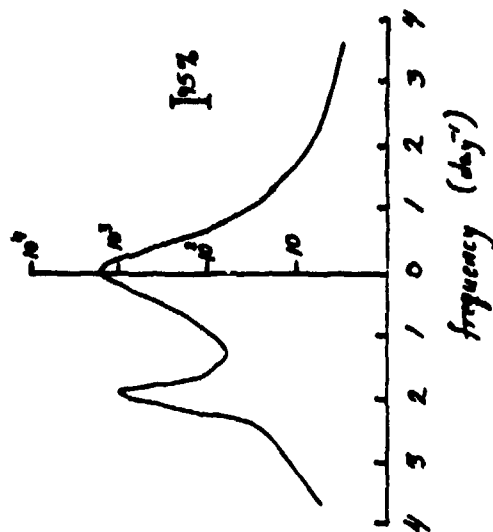
Figure 10. The power spectral density of the velocity of ice station Big Bear during summer 1975. The variance is 173 cm²sec⁻². (Linear frequency scale, from Colony and Thorndike, 1980.)
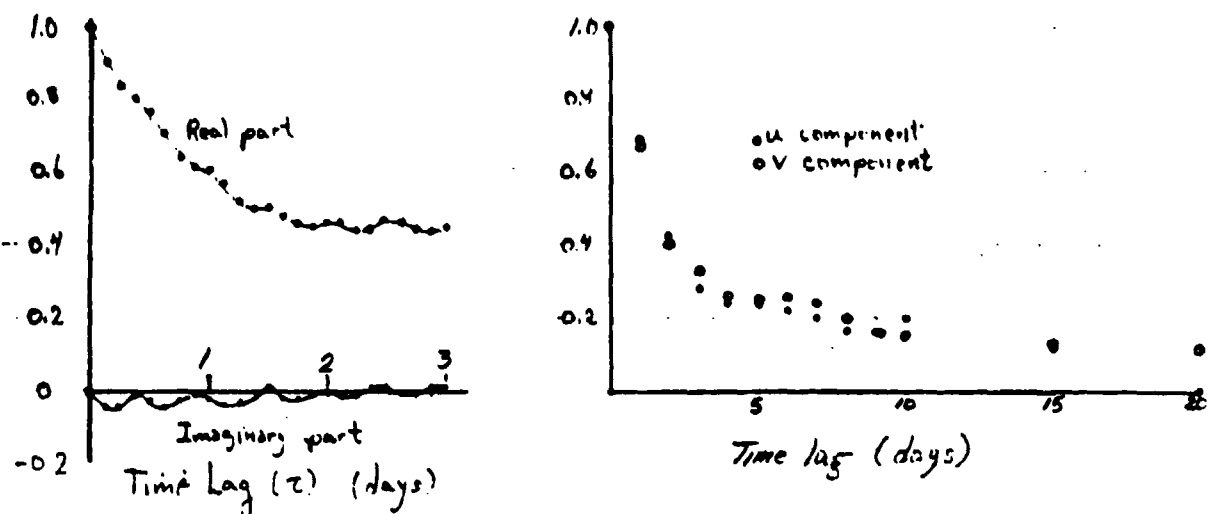
Figure 11. The complex time correlation function for ice station Caribou, 1975–76. The velocity variance is 145 cm^2 sec^{-2}.

Figure 12. The time correlation function for the u and v components of velocity from 28 grid points in the central part of the Arctic Basin, from drifting buoy data collected during 1979. The cross correlation between u and v is negligible. Variance of $u = 23$ cm^2 sec^{-2}; variance of $v = 22$ cm^2 sec^{-2}.
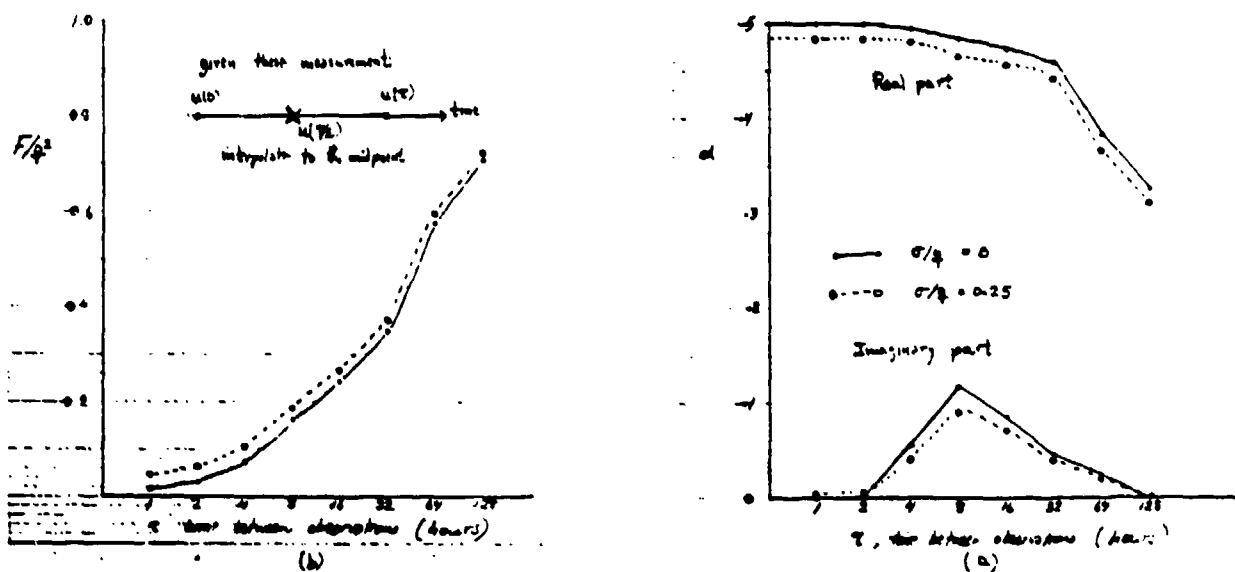
Figure 13. (a) The real and imaginary parts of the weight α to be used for inter-polating to the mid point of a time interval of duration τ. The ratio of the measurement error to the standard deviation of velocity is σ/ϕ. (b) The variance of the interpolation error expressed as a fraction of the variance of the ice velocity. Data from figure 11 were used here. Logarithmic time scale.
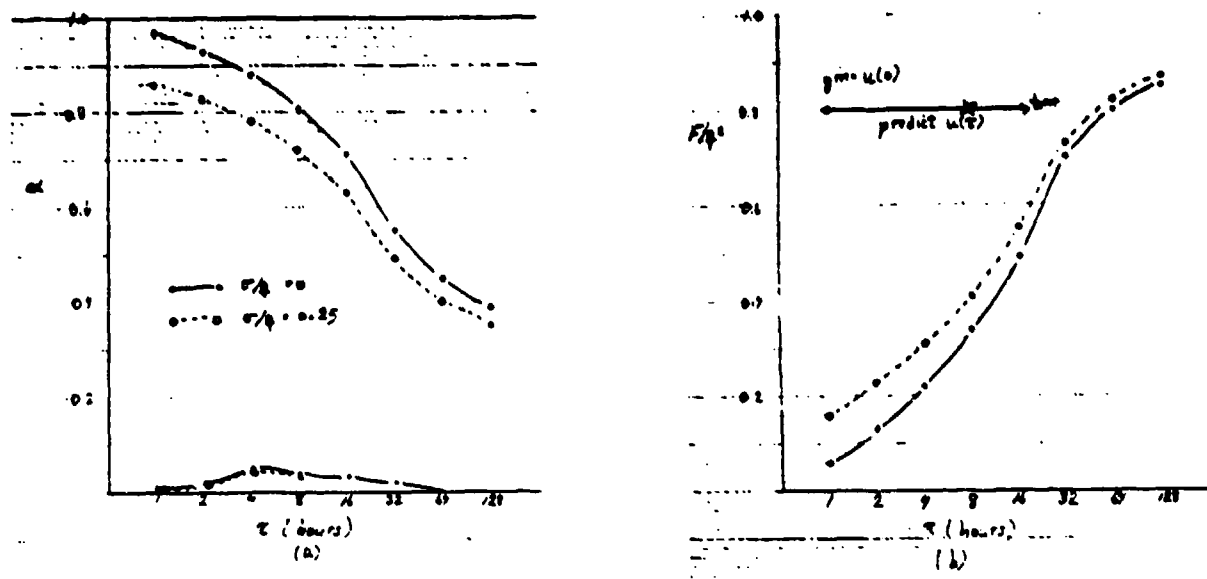
Figure 14. (a) The weight α for prediction over time τ.
(b) The prediction error variance versus prediction time. See Figure 13 also.
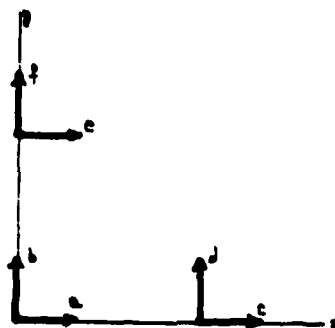
Figure 15. A schematic representation of the x and y components of velocity at the points (o,o), (τ,o), (o,τ). Isotropy implies $E_{ac} = E_{bf}$, $E_{bd} = E_{ae}$, and $E_{ce} = E_{df}$, but does not imply equality between E_{ac} and E_{ae} or E_{bf} and E_{bd}.
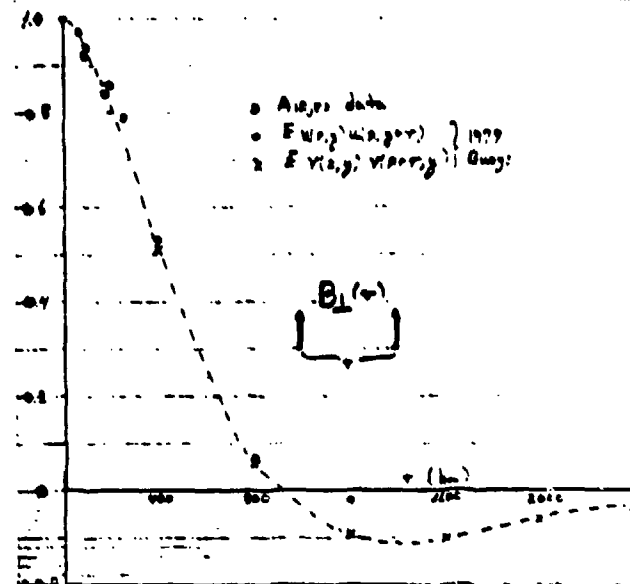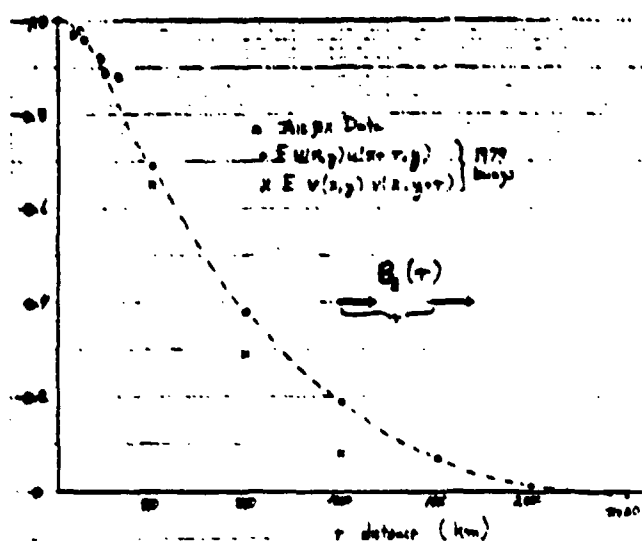
Figure 16. Observed correlations between velocity components as functions of distance.
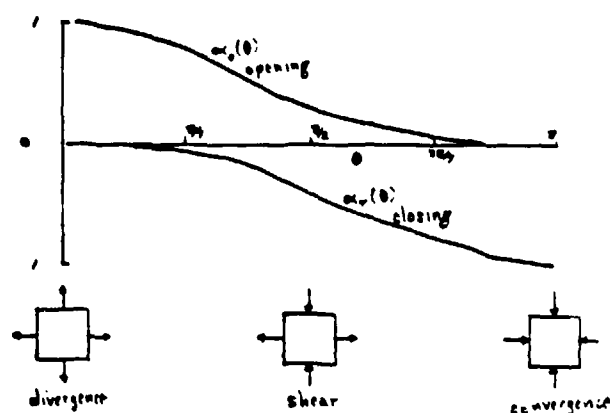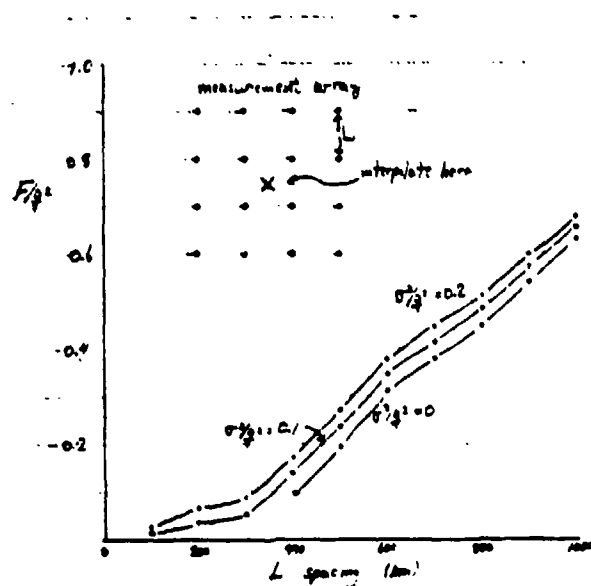
Figure 17. The variance of the interpolation error as a function of the grid spacing, L, and the measurement error, σ^2.

Figure 18. The strain rate invariant θ indicates whether the motion is dominated by divergence, shear, or convergence. The total opening and closing are sometimes treated as functions of θ.
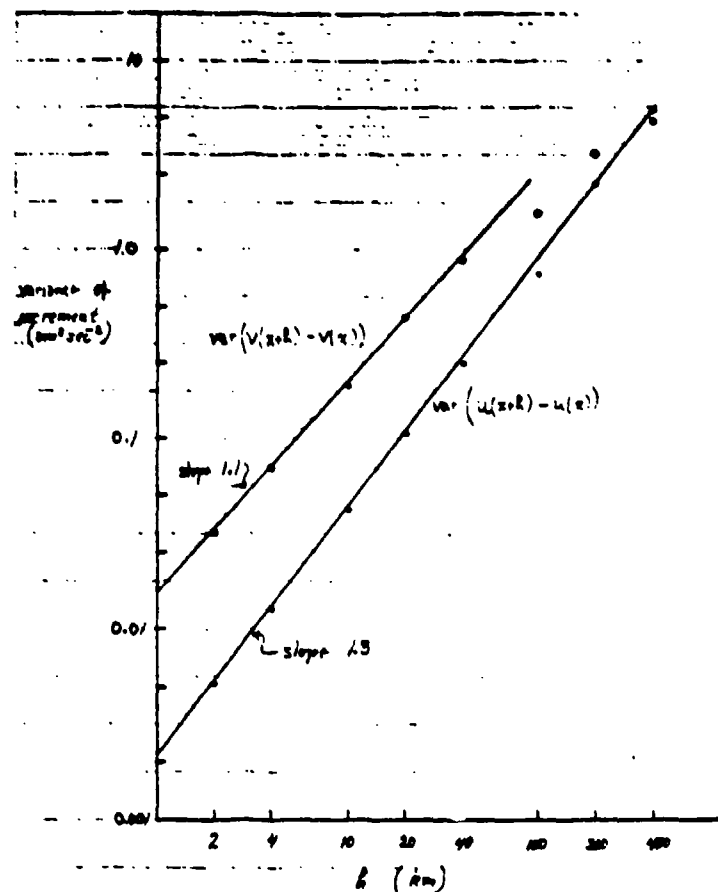
Figure 19. The variance of velocity increments versus interval length, from SeaSat
synthetic aperture radar data, 3-5 October 1978, Beaufort Sea.
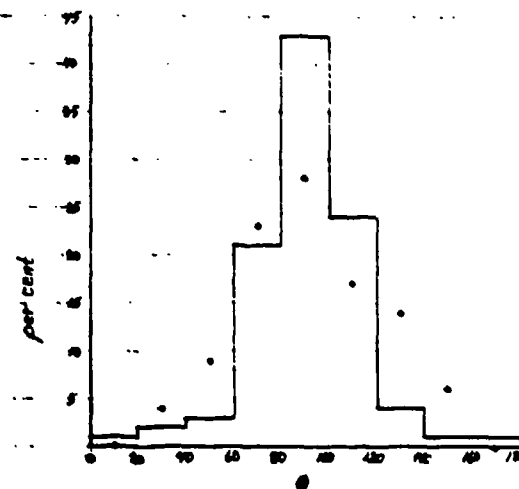
Figure 20. Histograms of the strain rate invariant θ . Solid line is for drifting
buoy data from 1979, grid spacing about 500 km (Colony and Thorndike, 1981).
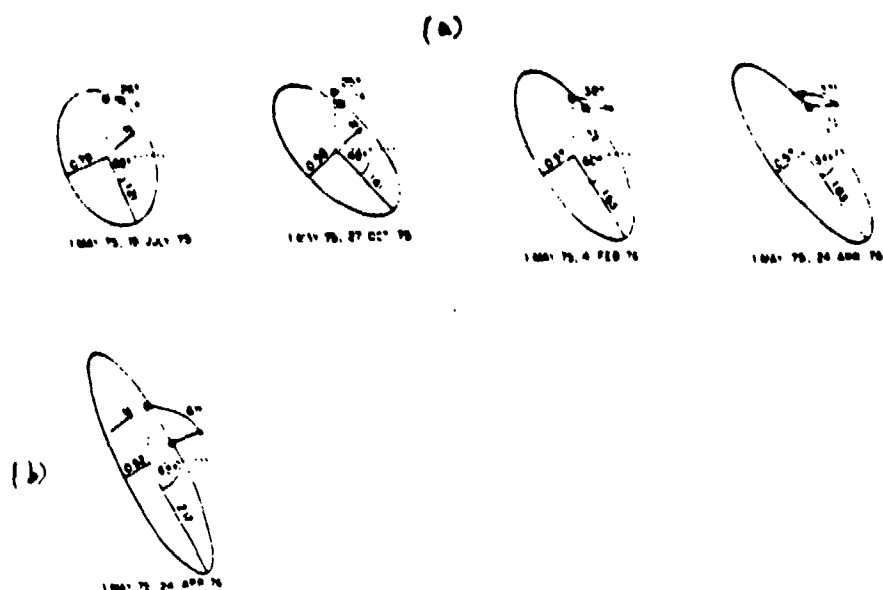Dots are for AIDJEX manned camp data, spacing 100 km (Nye, 1976).

(a)

(b)

Figure 21. Strain ellipses for the AIDJEX buoy array, 800 km diameter (a); and for the AIDJEX manned camp array, 200 km diameter (b). The ellipses show the deformation of a circular region on 1 May 1975, to the date indicated. The principal axes of the ellipse are the principal strains. The angle from the horizontal broken line to the major axis is the principal direction. The rigid body rotation is indicated by the arc from ☐ to *. Data from the Beaufort Sea, roughly a 500 km radius about 74°N, 145°W. (From Thorndike and Colony, 1980.)
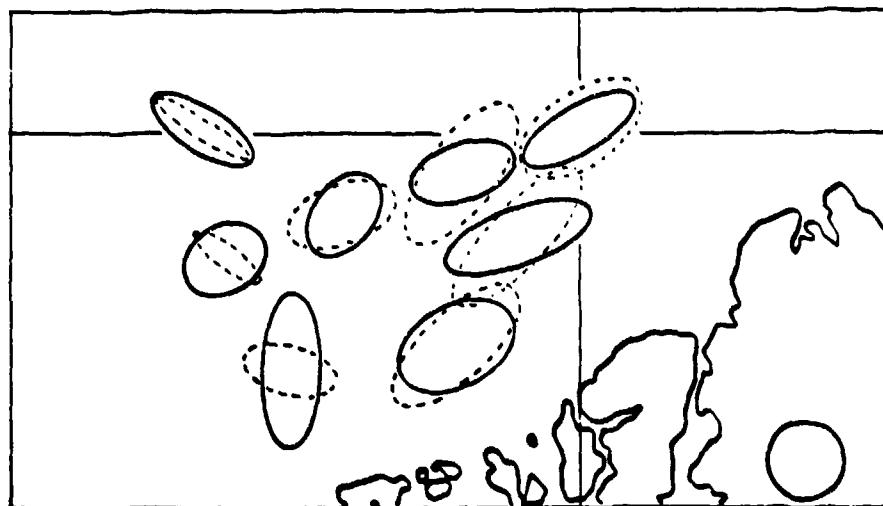
Figure 22. Strain ellipses from 1979 (solid line) and 1980 (broken line) drifting buoy data, showing the year long deformation of an initial circle (drawn over Greenland).
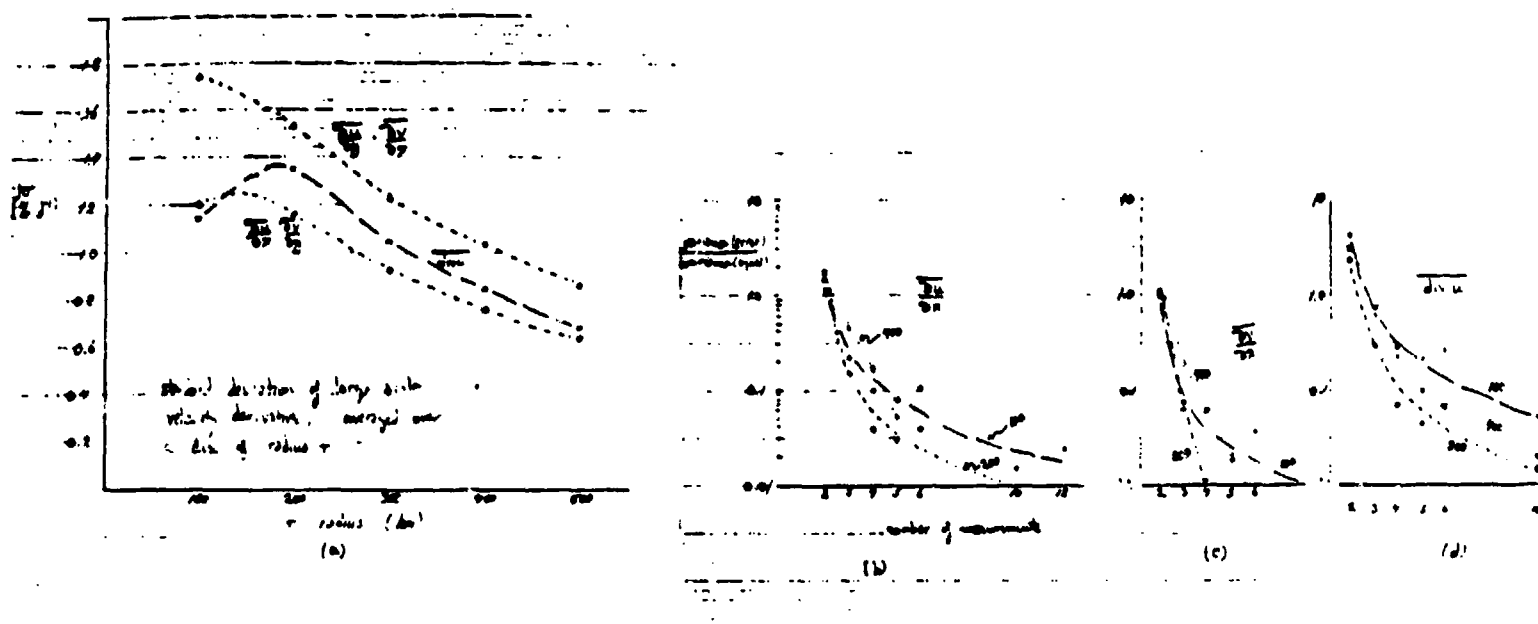
Figure 23. (a) Typical values for large scale average strain rate quantities are functions of the radius of the region over which the average is taken. (b) The estimation error for various average strain rate quantities depends on the radius of the region and on the number of measurements made around the perimeter.
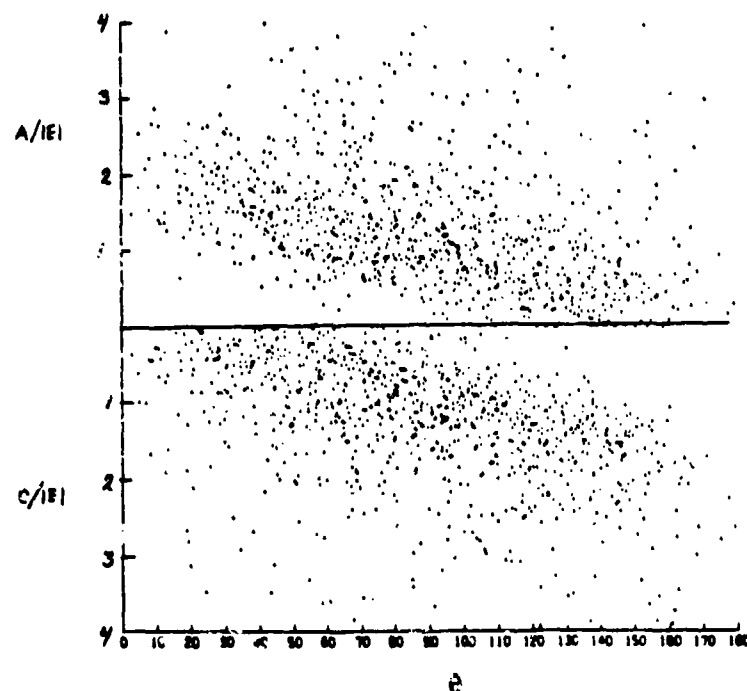

Figure 24. The total opening and closing versus ∂ . 10^5 realizations of the random field with Poisson parameter $\lambda L = 8$. The velocity discontinuities were drawn independently from the unit normal distribution.
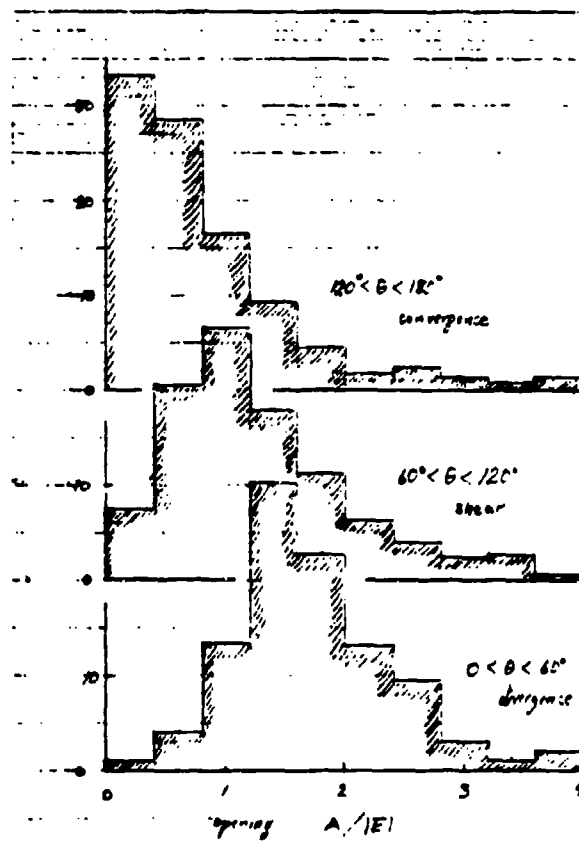
Figure 25. Distributions of the total opening for several ranges of θ. Data taken from figure 24.